

1 **Enhanced upward motion through the troposphere over the tropical**
2 **western Pacific and its implications for the transport of trace gases**
3 **from the troposphere to the stratosphere**

4 Kai Qie ¹, Wuke Wang^{2*}, Wenshou Tian ¹, Rui Huang¹, Mian Xu¹, Tao Wang¹,
5 Yifeng Peng¹

6
7 *¹College of Atmospheric Sciences, Lanzhou University, Lanzhou 730000, China*

8 *²Department of Atmospheric Science, China University of Geosciences, Wuhan*
9 *430074, China*

10
11
12 *Corresponding author: [Wuke Wang \(wangwuke@cug.edu.cn\)](mailto:wangwuke@cug.edu.cn)

13

14 **Abstract**

15 The tropical western Pacific (TWP) is a preferential area of air uplifting from the
16 surface to the upper troposphere. A significantly intensified upward motion through
17 the troposphere over the TWP in the boreal wintertime (November to March of the
18 next year, NDJFM) has been detected using multiple reanalysis datasets. The upward
19 motion over the TWP is intensified at rates of $8.0 \pm 3.1\%$ decade⁻¹ and $3.6 \pm 3.3\%$
20 decade⁻¹ in NDJFM at 150 hPa from 1958 to 2017 using JRA55 and ERA5 reanalysis
21 datasets, while the MERRA2 reanalysis data show a $7.5 \pm 7.1\%$ decade⁻¹ intensified
22 upward motion for the period 1980-2017. Model simulations using the Whole
23 Atmosphere Community Climate Model, version 4 (WACCM4) suggest that warming
24 global sea surface temperatures (SSTs), particularly SSTs over the eastern maritime
25 continent and tropical western Pacific, play a dominant role in the intensification of
26 the upward motion by strengthening the Pacific Walker circulation and enhancing the
27 deep convection over the TWP. Using CO as a tropospheric tracer, the WACCM4
28 simulations show that an increase of CO at a rate of 0.4 ppbv decade⁻¹ at the layer
29 150-70 hPa in the tropics is mainly resulted from the global SST warming and the
30 subsequent enhanced upward motion over the TWP in the troposphere and
31 strengthened tropical upwelling of Brewer-Dobson (BD) circulation in the lower
32 stratosphere. This implies that more tropospheric trace gases and aerosols from both
33 natural maritime source and outflow from polluted air from South Asia may enter the
34 stratosphere through the TWP region and affect the stratospheric chemistry and
35 climate.

36 **Keywords:** Upward motion; Troposphere-to-stratosphere transport; Tropical western

37 Pacific; Trend; Sea surface temperature

38

39

40 **1 Introduction**

41 The tropical western Pacific (TWP) is a critical region for tropical and global
42 climate (e.g., Webster et al., 1996; Hu et al., 2020). It has the largest area of warm sea
43 surface temperature (exceeding 28 °C) which fuels intense and massive deep
44 convection and thus is the largest source of latent heat and water vapor into the
45 atmosphere (Webster and Lukas, 1992). The TWP region is also the most important
46 source of tropospheric air entering the stratosphere due to the strong upward motion
47 and deep convection over this region (e.g., Fueglistaler et al., 2004; Pan et al., 2016).
48 Through the TWP region, tropospheric trace gases, e.g., the natural maritime
49 bromine-containing substances and outflow from anthropogenic emissions from South
50 Asia, are lifted to the upper troposphere and lower stratosphere (UTLS) by the strong
51 upward motion and the deep convection and subsequently into the stratosphere by the
52 large-scale upwelling (e.g., Levine et al., 2007, 2008; Navarro et al., 2015), which
53 affect the ozone concentration and other chemical processes in the stratosphere (e.g.,
54 Feng et al., 2007; Sinnhuber et al., 2009). At the same time, the TWP region has the
55 lowest cold-point tropopause temperature (CPTT) over the globe and plays an
56 important role in controlling the water vapor concentration in the stratosphere (e.g.,
57 Fueglistaler et al., 2009; Newell and Gould-Steward, 1981; Pan et al., 2016; Randel
58 and Jensen, 2013). The TWP is an important region for tropospheric trace gases being
59 transported from the troposphere to the stratosphere, and therefore influencing the
60 stratospheric chemistry (e.g., Fueglistaler et al., 2004; Levine et al., 2007; Krüger et

61 al., 2008; Pan et al., 2016).

62 The TWP was thought to be the main pathway of the troposphere-to-stratosphere
63 transport. A concept of “stratospheric fountain” was proposed by Newell and
64 Gould-Steward (1981), which suggested that the poor-water vapor air in the
65 stratosphere stems mainly from the TWP region. However, following studies using the
66 observational and reanalysis data showed that there is subsidence at the
67 near-tropopause level over the maritime continent, which is named as the
68 “stratospheric drain” (Gettelman et al., 2000; Sherwood, 2000; Fueglistaler et al.,
69 2004). Further studies verified that the large-scale transport from the tropical
70 tropopause layer (TTL) to the stratosphere is dominated by the upward branch of the
71 Brewer-Dobson (BD) circulation (Brewer, 1949; Dobson, 1956; Holton et al., 1995)
72 while the local upwelling may play a minor role (e.g., Levine et al., 2007; Fueglistaler
73 et al., 2009; Schoeberl et al., 2018).

74 Though the vertical transport from TTL to the lower stratosphere is dominated by
75 the BD circulation, numerous studies confirmed that the TWP region is an important
76 pathway of the surface air entering the TTL (Fueglistaler et al., 2004; Levine et al.,
77 2007; Krüger et al., 2008; Haines and Esler, 2014). Based on a trajectory model,
78 Fueglistaler et al. (2004) pointed out that approximately 80% of the trajectories
79 ascending into the stratosphere from the TTL are originated from the TWP region.
80 Bergman et al. (2012) suggested that the tropospheric air over the TWP enters the
81 stratosphere mainly in boreal winter, while less air over the TWP could be transported
82 into the stratosphere during boreal summer. Other studies also found that the TWP

83 region is an important source of the tropospheric trace gases in the TTL (e.g., Newton
84 et al., 2018; Pan et al., 2016; Wales et al., 2018), even the polluted air from East Asia
85 could be transported rapidly to Southeast Asia by meridional winds and subsequently
86 be elevated to the tropical upper troposphere by the strong upward motion and the
87 deep convection (Ashfold et al., 2015). Hence, the strength of the upward motion over
88 the TWP region during boreal winter is a key feature for understanding the variations
89 of trace gases in the TTL and therefore important for stratospheric chemistry and
90 climate.

91 The strength of the TWP upward motion is closely related to atmospheric
92 circulation and deep convection. The ascending branch of the Pacific Walker
93 circulation and the strong deep convection over the TWP allow rapid transport from
94 the surface to the upper troposphere (Hosking et al., 2012). In association with global
95 warming, atmospheric circulation, deep convection as well as the boundary conditions
96 (e.g., sea surface temperature; SST) have been changed. For example, the Hadley cell
97 has been extended to the subtropics and the Walker circulation over the Pacific has
98 been shifted westward over the past decades (e.g., Lu et al., 2007; Garfinkel et al.,
99 2015; Ma and Zhou, 2016). At the same time, SSTs over most of areas are getting
100 warmer (Cane et al., 1997; Deser et al., 2010), which modulates the deep convection
101 and atmospheric wave activities in the troposphere and then lead to changes of
102 atmospheric circulations from the troposphere and the stratosphere (e.g., Garfinkel et
103 al., 2013; Xie et al., 2012, 2014a; Wang et al., 2015; Hu et al., 2016; Lu et al., 2020).
104 However, how the strength of the upward motion in the lower TTL over the TWP

105 region has been changed over the past decades remains unclear. In this study, we
106 investigate the long-term trend of the upward motion over the TWP using JRA55,
107 ERA5, and MERRA2 reanalysis datasets and different WACCM4 simulations as
108 described in Section 2. The implication of the changes in the upward motion over the
109 TWP to the transport of trace gases from the surface to the UTLS will be discussed in
110 Section 3.

111 **2 Data and method**

112 **Reanalysis data.** To investigate the long-term trend of the upward motion over
113 the TWP through the troposphere, three most recent reanalysis datasets, including
114 JRA55 from the Japan Meteorological Agency (JMA), ERA5 from the European
115 Centre for Medium Range Weather Forecasting (ECMWF) and MERRA2 from the
116 National Aeronautics and Space Administration/Global Modeling and Assimilation
117 Office (NASA/GMAO) are used in this study ([Table 1](#)). [The JRA55 data, covering the](#)
118 [period from 1958 to present, are interpolated to the standard pressure levels and](#)
119 [1.25°×1.25° horizontal mesh](#) (Harada et al. 2016). The ERA5 reanalysis is the newest
120 generation product from the ECMWF (Hersbach et al., 2020). The ERA5 data are
121 based on the Integrated Forecasting System (IFS) Cy41r2, which includes the
122 improved model physics, core dynamics and data assimilation. The ERA5 data also
123 extend back to 1958, which is coinciding with the time that radiosonde observations
124 in the Arctic became more systematic and regular. It should be noted that the ERA5
125 data suffer from a bias during 2000-2006, and are replaced by the ERA5.1 data in this
126 period here. The MERRA2 data are also used ([Gelaro et al., 2017](#)), which are

127 produced by NASA/GMAO using Goddard Earth Observing System model (GEOS).
128 Although the horizontal and vertical resolution of MERRA2 data are similar to
129 MERRA data, the MERRA2 data represent UTLS processes better (Gelaro et al.,
130 2017). The monthly mean air temperature, horizontal wind fields and vertical velocity
131 at different pressure levels are extracted from the three Reanalysis datasets. In the
132 present study, we mainly focus on the upward motion over TWP region in NDJFM,
133 which is defined as 20°S-10°N, 100°E-180° due to the strong upward motion (Fig. 1)
134 and significantly increasing trends of the upward motion (Fig. 2) over there.

135 A special caution is needed because of the limitations of reanalysis data. The
136 reanalysis datasets assimilate observational data based on the ground- and
137 space-based remote sensing platforms to provide more realistic data products.
138 However, previous studies suggested that there are still uncertainties in the reanalysis
139 data (e.g., Simmons et al., 2014; Long et al., 2017; Uma et al., 2021). The accuracy of
140 the vertical velocity in reanalysis data sets has been evaluated by the Reanalysis
141 Intercomparison Project (Fujiwara et al., 2017), which is initiated by the
142 Stratosphere-troposphere Processes And their Role in Climate (SPARC). Results of a
143 comparison between the radar observed data and the reanalysis data indicate that the
144 updrafts in the UTLS are captured well near the TWP even though there are still large
145 biases in the reanalysis datasets and the updrafts from the JRA55 data are stronger
146 than those from the ERA5 and MERRA2 data (Uma et al. 2021). Additionally,
147 discontinuities in the reanalysis data due to different observing systems (for example,
148 transition from TOVS to ATOVS) may still exist (e.g., Long et al., 2017), which could

149 lead to uncertainties in the long-term trend of a certain meteorological field.
150 Hitchcock (2019) suggested that the reanalysis uncertainty is larger in the radiosonde
151 era (after 1958) than in the satellite era (after 1979), but the radiosonde era is of
152 equivalent value to the satellite era because the dynamical uncertainty dominates in
153 the both eras. The data in the radiosonde era (1958-1978) used in the present study
154 may induce uncertainties in our results. Therefore, we discuss the trends for both the
155 periods of 1958-2017 and 1980-2017. In addition, we combine three most recent
156 reanalysis datasets (JRA55, ERA5, and MERRA2) to obtain relatively robust results.

157 **Observed CO data.** Since CO has a photochemical lifetime in the range of 2-3
158 months (Xiao et al., 2007), it could be utilized as a tracer of cross-region transport in
159 the troposphere and the lower stratosphere (Park et al., 2009). Here, CO is used as a
160 tropospheric tracer to indicate the vertical transport from the near-surface to the upper
161 troposphere and the lower stratosphere. The CO data used in the present study are
162 from space-borne Microwave Limb Sounder (MLS; Livesey et al., 2015) observation
163 and Measurements Of Pollution In The Troposphere instrument (MOPITT; Deeter et
164 al., 2019). MLS is carried by Aura, which has a sun-synchronous orbit at 705 km with
165 a 16-day repeat cycle. MLS observations are made from 82°S to 82°N and cover the
166 period from 2005 to the present. MLS provides the CO data from the upper
167 troposphere to the mesosphere. MLS CO v4 level1 data used in the present study are
168 processed using the recommended procedures (Livesey et al., 2015) and interpolated
169 into a 5°×5° horizontal mesh. MOPITT CO data are also used for comparison.
170 MOPITT instrument is aboard on the Terra satellite permitting retrievals of CO

171 vertical profiles using both thermal-infrared and near-infrared measurements and has
172 a field of view of 22 km×22 km. The Terra satellite was launched in 1999 with a 705
173 km sun-synchronous orbit. MOPITT provides the CO data from the surface to the
174 upper troposphere during the period of 2000/03 to the present. Here, we use the
175 daytime only MOPITT v8 level3 CO data. For comparison, we focus on the CO
176 concentrations in MLS and MOPITT data at similar level (215 hPa in MLS data and
177 200 hPa in MOPITT data, respectively).

178 **SST and outgoing longwave radiation (OLR) data.** SST data are used in this
179 study to investigate the relationship between the upward motion and SSTs. The SST
180 data are from the HadISST dataset ($1^{\circ}\times 1^{\circ}$ horizontal mesh) during 1958-2018
181 (Rayner et al., 2003). OLR is often utilized to reflect the deep convection in the
182 tropics. The OLR data are extracted from NOAA Interpolated OLR dataset on a
183 $2.5^{\circ}\times 2.5^{\circ}$ horizontal mesh during 1974/11-2018/03 (Liebmann and Smith, 1996).

184 **Model simulations.** A series of model simulations with the Whole Atmosphere
185 Community Climate Model version 4 (WACCM4) are performed to find out the main
186 impact factors of the trend of the upward motion over the TWP [\(Table 2\)](#). The
187 WACCM4 is a chemical-climate model with a horizontal resolution of $1.9^{\circ}\times 2.5^{\circ}$
188 (Marsh et al., 2013). The WACCM4 has vertical 66 levels from the surface to 145 km
189 with vertical resolution of approximately 1 km in the UTLS, which is numerously
190 used to investigate the transport of the trace gases from the troposphere to the
191 stratosphere (e.g., Randel et al., 2010; Xie et al., 2014b; Minganti et al., 2020). A
192 hindcast simulation (Control simulation) is performed with observed greenhouse

193 gases, solar irradiances, and prescribed SSTs (HadISST dataset is used) during
194 1955-2018. A single-factor controlling simulation (Fixsst simulation) is done for the
195 same period with the same forcings, except that the global SSTs are fixed to the
196 climatological mean values during 1955-2018 (long-term mean for each calendar
197 month during 1955-2018).

198 To figure out the impact of the warming SST over the TWP region on the
199 intensification of the upward motion over the TWP region, a couple of time-slice
200 simulations (R1 and R2) are also integrated for 33 years. The SSTs over the eastern
201 maritime continent and tropical western Pacific (20°S - 20°N , 120°E - 160°E) in the
202 boreal wintertime (November to March of the next year, NDJFM) in R1 are
203 prescribed as the climatological mean SSTs during 1998-2017, while the SSTs over
204 other regions are fixed as the climatological mean SSTs during 1958-2017. The SSTs
205 in R2 are the same as the SSTs in R1 except that the SSTs over the region (20°S - 20°N ,
206 120°E - 160°E) in NDJFM are prescribed as the climatological mean SSTs during
207 1958-1977. Since the SSTs over the eastern maritime continent and tropical western
208 Pacific (20°S - 20°N , 120°E - 160°E) show significantly warming trends, the SSTs
209 during 1998-2017 are higher than the SSTs during 1958-1977 (approximately 0.5 K).
210 Hence, the difference between R1 and R2 reflects the impact of the warmed SSTs
211 over the eastern maritime continent and tropical western Pacific (20°S - 20°N ,
212 120°E - 160°E) on the atmospheric circulation. The first 3 years of the numeric
213 simulations are not used in the present study to provide a spin-up.

214 **Transformed Eulerian Mean (TEM) calculation.** To diagnose the changes in

215 the BD circulation, the meridional and vertical velocities of the BD circulation are
 216 calculated by the TEM equations (Andrews and McIntyre, 1976):

$$217 \quad v^* = \bar{v} - \frac{1}{\rho} \left(\frac{\overline{\rho v' \theta'}}{\theta_z} \right)_z$$

$$218 \quad w^* = \bar{w} + \frac{1}{a \cos \varphi} \left(\cos \varphi \frac{\overline{v' \theta'}}{\theta_z} \right)_\varphi$$

219 Where v^* and w^* denote the meridional and vertical velocities of the BD circulation;
 220 the overbar represents the zonal mean; the prime denotes the deviation from the zonal
 221 mean; θ , a , φ , and ρ indicate the potential temperature, the radius of the earth,
 222 the latitude, and the standard density.

223 **Linear trends and the significance test.** The linear trends are estimated using a
 224 simple least square regression method. The significances of the correlation
 225 coefficients, mean differences, and trends are determined via a two-tail Student's t-test.

226 The confidence interval of trend is calculated using the following equation (Shirley et

$$227 \text{ al., 2004): } \left(b - t_{1-\frac{\alpha}{2}}(n-2)\sigma_b, b + t_{1-\frac{\alpha}{2}}(n-2)\sigma \right)$$

228 where b is the estimated slope, σ denotes the standard error of the slope, and
 229 $t_{1-\frac{\alpha}{2}}(n-2)$ represents the value of t-distribution with the degree of freedom equal to

$$230 \quad n-2. \alpha \text{ is the two-tailed confidence level. } \sigma \text{ is calculated as: } \sigma = b \sqrt{\frac{1}{r^2} - 1}.$$

231 **3 Results**

232 **3.1 Enhanced upward motion over the TWP**

233 According to previous studies, the lapse-rate tropopause is a good proxy to
 234 separate the tropospheric and the stratospheric dynamic behavior (vertical motion

235 dominated and horizontal mixing dominated, respectively) over the TWP (Pan et al.,
236 2019). Since the lapse-rate tropopause over the TWP in the boreal winter is near 100
237 hPa (not shown), we utilize the vertical velocity at 150 hPa to reflect the vertical
238 transport in the upper troposphere. Figure 1 shows mean values of the vertical
239 velocity at 150 hPa for each month averaged over 60 years from 1958 to 2017. The
240 TWP region at the UTLS level has strong upward motion due to the frequent intense
241 deep convection and the Pacific Walker circulation. It is noteworthy that there is
242 strong upward motion at 150 hPa in NDJFM over the TWP, while the upward motion
243 in other months shifts northward corresponding to the Asia summer monsoon. This is
244 consistent with previous studies (Newell and Gould-Steward, 1981; Bergman et al.,
245 2012). Therefore, we mainly focus on the changes in the upward motion in NDJFM,
246 which is more important to the transport of air over the TWP from the lower
247 troposphere to the TTL compared to the summer months (as shown in Fig. 1) and
248 subsequently to the lower stratosphere. As seen in Figs. 1a-c and 1k-l, the upward
249 motion (w) at 150 hPa is most evident over the region 20°S - 10°N , 100°E - 180° , which
250 is used to indicate the TWP in the following analysis. The climatological mean 150
251 hPa vertical velocity (w) in NDJFM in ERA5 during 1958-2017 and MERRA2 during
252 1980-2017 are also given in Supplementary Fig. 1. Comparing with the 150 hPa w in
253 NDJFM using JRA55, the 150 hPa w in ERA5 and MERRA2 data shows larger
254 values (maximum larger than 1.5 cm s^{-1}) over the land areas but smaller values
255 (minimum less than -0.4 cm s^{-1}) over the marine area. Notably, the 150 hPa w shows
256 no subsidence over the maritime continent, while there is descending motion over the

257 maritime continent at 100 hPa (Supplementary Fig. 2), which is referred to the
258 “stratospheric drain” (Gettleman et al., 2000; Sherwood, 2000).

259 Figure 2 displays the linear trends of w in the upper (150 hPa), middle (500 hPa)
260 and lower (700 hPa) troposphere in NDJFM from 1958 to 2017 using JRA55, ERA5,
261 and MERRA2 reanalysis datasets. The 150 hPa w increased significantly over most
262 areas of the TWP during 1958-2017 (Fig. 2). At the same time, the upward motion
263 over the TWP in the lower and middle troposphere also mainly shows positive trends
264 (Figs. 2d and g). This indicates that the upward motion over the TWP is increasing
265 through the troposphere from 1958 to 2017. Such an enhancement of the upward
266 motion over the TWP is evident in all three reanalysis datasets used here (JRA55,
267 ERA5, and MERRA2), although there are also some differences between the three
268 reanalysis datasets. For example, the trends of the horizontal winds in the upper
269 troposphere in MERRA2 (Fig. 2c) are larger than those in JRA55 and ERA5 (Figs. 2a
270 and b). There are negative trends of vertical velocity in JRA55 and ERA5 while
271 positive trends of vertical velocity in MERRA2 over the northern Pacific. However,
272 these differences are mainly due to the different time periods which are used to
273 calculate the linear trends in JRA55 (1958-2017), ERA5 (1958-2017) and MERRA2
274 (1980-2017). Supplementary Fig. 3 gives the trends of w and horizontal winds in
275 NDJFM during 1980-2017 derived from JRA55, ERA5, and MERRA2 data, which
276 shows insignificant differences between these reanalysis datasets. The trend patterns
277 of the horizontal winds in JRA55, ERA5, and MERRA2 are consistent with each
278 other (Supplementary Fig. 3). For the trends of vertical velocity, significantly positive

279 trends over the TWP region can be noted in the JRA55, ERA5, and MERRA2 datasets,
280 although the trends in ERA5 are slightly weaker than those in JRA55 and MERRA2
281 (Fig. 2 and Supplementary Fig. 3). Comparing to the negative trends of the vertical
282 velocity over the central Pacific in JRA55 and ERA5, the negative trends in MERRA2
283 extend more northward (Supplementary Fig. 3).

284 The time series of the upward motion intensity over the TWP from different
285 datasets are given in Fig. 3. The intensity of the upward motion over the TWP used in
286 Fig. 3 is simply defined as the area-averaged upward mass flux at a specific level, and
287 the standardized intensity is calculated as the intensity divided by the standard
288 deviation of the intensity at the corresponding level. The intensity of the upward
289 motion over the TWP at 150 hPa increased significantly in NDJFM during last
290 decades, which can be confirmed by all the three reanalysis datasets (Fig. 3). The
291 intensity of the upward motion over the TWP at 150 hPa increased $3.0 \pm 1.2 \times 10^9 \text{ kg s}^{-1}$
292 decade^{-1} ($8.0 \pm 3.1\% \text{ decade}^{-1}$), $1.3 \pm 1.2 \times 10^9 \text{ kg s}^{-1} \text{ decade}^{-1}$ ($3.6 \pm 3.3\% \text{ decade}^{-1}$), and
293 $3.0 \pm 2.8 \times 10^9 \text{ kg s}^{-1} \text{ decade}^{-1}$ ($7.5 \pm 7.1\% \text{ decade}^{-1}$) in JRA55, ERA5, and MERRA2 data,
294 respectively (Table 3). As shown in Figs. 3b and c, the intensity of the upward motion
295 at 500 hPa and 700 hPa in JRA55 and the intensity of the upward motion at 500 hPa
296 in ERA5 over the TWP also increased significantly at 95% confidence level
297 ($4.6 \pm 2.6 \times 10^9 \text{ kg s}^{-1} \text{ decade}^{-1}$, $2.9 \pm 1.7 \times 10^9 \text{ kg s}^{-1} \text{ decade}^{-1}$, and $2.5 \pm 2.5 \times 10^9 \text{ kg s}^{-1}$
298 decade^{-1} , respectively). The increasing trends of the intensity of the upward motion at
299 700 hPa in ERA5 and at 500 hPa and 700 hPa in MERRA2 are significant at the 90%
300 confidence level at rates of $1.9 \pm 1.6 \times 10^9 \text{ kg s}^{-1} \text{ decade}^{-1}$, $5.4 \pm 5.3 \times 10^9 \text{ kg s}^{-1} \text{ decade}^{-1}$

301 and $3.9\pm 3.8\times 10^9$ kg s⁻¹ decade⁻¹, respectively. This suggests a comprehensive
302 enhancement of vertical velocity through the whole troposphere, which is evident
303 from the surface to 100 hPa (Supplementary Fig. 4). It can also be inferred that the
304 upward motions over the TWP increased at different rates during the past decades due
305 to the difference between JRA55, ERA5, and MERRA2 data. Hence, caution is
306 suggested when investigating the trend of the upward motion over the TWP using the
307 reanalysis data. While the trace gases in the TTL are modulated by the upward motion
308 and subsequent vertical transport (e.g., Garfinkel et al., 2013; Xie et al., 2014b), such
309 a strengthening of the upward motion over the TWP may lead to more tropospheric
310 trace gases in the TTL.

311 The changes in the atmospheric circulation at the UTLS level in the tropics are
312 closely related to the changes in the tropical deep convection and SSTs (e.g., Levine
313 et al., 2008; Garfinkel et al., 2013; Xie et al., 2020). Here, the trends of observed OLR
314 provided by NOAA (see Section 2) in NDJFM during 1974-2017 are shown in Fig. 4a.
315 Though the time period of the observed OLR data is shorter than the time period we
316 analyzed, the changes in OLR could partly reflect the changes in the deep convection
317 during 1958-2017. The OLR shows significantly negative trends over the TWP which
318 indicates intensified deep convection over the TWP. The OLR trend pattern is very
319 similar to the trend pattern of the 150 hPa w (Figs. 2a-c), which indicates that the
320 increasing trends of 150 hPa w are closely related to the intensified deep convection
321 over the TWP. The intensified deep convection not only lead to the strengthened
322 upward motion in the UTLS (Highwood and Hoskins, 1998; Ryu and Lee, 2010), but

323 also result in the decreased temperature near the tropopause which plays a dominant
324 role in modulating the lower stratospheric water vapor concentration (e.g., Hu et al.,
325 2016; Wang et al., 2016). Corresponding to the enhanced deep convection over the
326 TWP, the CPTT derived from JRA55 data (see Fig. 4b) shows significantly decreasing
327 trends over the TWP in NDJFM during 1958-2017, which is consistent with Xie et al.,
328 (2014a). However, negative trends are also found in other regions in low and
329 mid-latitudes, except over the central and east Pacific. It should be noted that the
330 CPTT from different reanalysis datasets may show different trends even for the
331 satellite period (Tegtmeier et al., 2020). Additionally, the JRA55 data before 1978
332 may also lead to uncertainties in the CPTT trends. Caution is needed when discussing
333 the trends of CPTT from reanalysis datasets.

334 The changes in the deep convection over the tropical Pacific may be related to
335 the changes in the Pacific Walker circulation. The Pacific Walker circulation shows a
336 significant intensification over the past decades (e.g., Meng et al., 2012; L'Heureux et
337 al., 2013; McGregor et al., 2014). The vertical velocity at 500 hPa and 150 hPa shows
338 significantly positive trends over the TWP in NDJFM during 1958-2017 (Fig. 2).
339 Meanwhile, the lower tropospheric zonal wind shows easterly trends over the tropical
340 Pacific, while the upper tropospheric zonal wind shows westerly trends over the
341 tropical Pacific, which suggests a strengthened Pacific Walker circulation and is
342 consistent with previous studies (Hu et al., 2016; Ma and Zhou, 2016).

343 The strengthened Pacific Walker circulation is closely related to the changes in
344 the SSTs (e.g., Meng et al., 2012; Ma and Zhou, 2016). The trends of the SSTs in

345 NDJFM during 1958-2017 are shown in Fig. 4c. The SST shows significantly
346 warming trends almost over the world except the central Pacific in NDJFM during
347 1958-2017. In addition, the intensity of the upward motion over the TWP is
348 significantly correlated with the SST (Fig. 4d), which suggests that the SST has
349 important effects on the upward motion over the TWP. The correlation coefficient in
350 Fig. 4d shows a La Niña-like pattern and indicates that the ENSO events exert
351 important impacts on the upward motion over the TWP (Levine et al., 2008). The
352 SSTs over the TWP are mainly positively correlated with the upward motion intensity
353 over the TWP with negative correlations shown over the western maritime continent,
354 while the SSTs over tropical central, eastern Pacific, and Indian Ocean show negative
355 correlations with the intensity of the upward motion over the TWP. The SSTs over the
356 Atlantic Ocean are poorly correlated with the upward motion intensity over the TWP
357 (not shown). This result suggests that the changes in global SSTs may be the primary
358 driver of the strengthened Pacific Walker circulation, which leads to enhanced deep
359 convection and intensified upward motion over the TWP.

360 It could be found that there are extreme minima (1982, 1991, and 1997) in Fig. 3,
361 which may be related to the El Niño events occurred in these years. To further figure
362 out the impact of ENSO events on the upward motion over the TWP, Supplementary
363 Fig. 5 displays the time series of the standardized intensity of the upward motion over
364 the TWP at 150 hPa, 500 hPa, and 700 hPa in NDJFM in JRA55, ERA5, and
365 MERRA2 with the ENSO signal removed using the linear regression method (Hu et
366 al., 2018; Qie et al., 2021). The extreme minima (1982, 1991, and 1997) become

367 much weaker in Supplementary Fig. 5 than those in Fig. 3, which indicates that the El
368 Niño events are responsible for the extreme minima. The upward motions over the
369 TWP at 150 hPa, 500 hPa, and 700 hPa in NDJFM in JRA55, ERA5, and MERRA2
370 still show statistically significant increasing trends after removing the ENSO signal in
371 Supplementary Fig. 5, which suggests that ENSO events exert limited impacts on the
372 trends of the upward motion over the TWP in NDJFM during 1958-2017.

373 **3.2 Simulated trend of the upward motion over the TWP and its potential** 374 **mechanism**

375 To verify the impact of SST on the trend of the upward motion over the TWP, a
376 couple of model simulations with WACCM4 are employed in the following analysis.
377 Consistent with the results shown using the reanalysis data (Figs. 2a-c), the simulated
378 150 hPa w (Control simulation) shows significantly increasing trends over the TWP
379 and decreasing trends over the tropical eastern Pacific in NDJFM during 1958-2017
380 (Fig. 5a). Additionally, the 150 hPa w simulated in the Fixsst simulation shows weak
381 trends over the TWP (Fig. 5b). The difference between the Control and the Fixsst
382 simulations suggests that the trends of the 150 hPa w over the TWP region is
383 dominated by the changes in the global SSTs during 1958-2017. There are also
384 significantly positive trends of the vertical velocity over the TWP in the lower (700
385 hPa) and middle troposphere (500 hPa) in the Control simulation, while the zonal
386 winds are also enhanced over the tropical Pacific. The vertical velocity over the TWP
387 in the Fixsst simulation shows weak negative trends and the changes in zonal winds
388 over the tropical Pacific are very weak. This confirms the dominant role of the

389 changes in global SSTs on the enhancement of the Walker circulation.

390 Previous studies found that the changes in the intensity of the Pacific Walker
391 circulation and the stratospheric residual circulation are closely related to the changes
392 in tropical SST (Meng et al., 2012; Tokinaga et al., 2012; Lin et al., 2015). As
393 suggested by the correlation coefficients between the upward motion at 150 hPa over
394 the TWP and SSTs in Fig. 4d, warmer SSTs over the tropical central and eastern
395 Pacific, and Indian Ocean may lead to a weakened upward motion over the TWP
396 (negative correlation). The warming trends of SSTs over the eastern maritime
397 continent and tropical western Pacific may result in an intensification of the upward
398 motion over the TWP. To verify the impact of the changes in the SSTs over eastern
399 maritime continent and tropical western Pacific on the trends of the upward motion
400 over the TWP, a couple of single-factor controlling time-slice simulations (R1 and R2)
401 are performed with only SSTs over eastern maritime continent and tropical western
402 Pacific (20°S-20°N, 120°E-160°E) in NDJFM changed in these two simulations. In
403 R1, the SSTs over the eastern maritime continent and tropical western Pacific are
404 prescribed as the climatological mean SSTs during 1958-2017, while the SSTs over
405 the eastern maritime continent and tropical western Pacific in R2 are prescribed as the
406 climatological mean SSTs during 1958-1977 (more details are given in the section 2).
407 The differences of the wind fields between R1 and R2 are shown in Fig. 6. The 150
408 hPa w shows significantly positive anomalies over the TWP and negative anomalies
409 over the tropical eastern Pacific, which is consistent with the trends of the 150 hPa w
410 in the Control simulation and the reanalysis datasets (Figs. 2 and 5). The upward mass

411 flux over the TWP at 150 hPa increased approximately 27% in the R1 comparing with
412 R2 due to the warming SSTs over the eastern maritime continent and tropical western
413 Pacific (approximately 0.5 K). The upward motion in the lower and middle
414 troposphere over the TWP shows increasing trends due to the enhanced convergence
415 induced by the warmer SSTs over the TWP. This result is consistent with Hu et al.
416 (2016), which suggested that the increased zonal gradient of the SSTs over the
417 tropical Pacific could lead to a strengthened Pacific Walker circulation and an
418 enhanced upward motion over the TWP. Therefore, the warmer SSTs over the TWP
419 could contribute largely to the trend of the upward motion over the TWP in NDJFM
420 during 1958-2017.

421 The changes in the OLR simulated in WACCM4 associated with the changes in
422 the global SSTs are shown in Fig. 7. There are significantly enhanced deep convection
423 as indicated by OLR over the TWP due to the strengthened convergence in the
424 Control simulation, while the deep convection shows weak and even decreasing
425 trends over the TWP in the Fixsst simulation (Figs. 7a and b). The enhanced deep
426 convection over the TWP could lead to the enhancing trends of the upward motion.
427 Hence, it can be inferred that the changes in the global SSTs are responsible for the
428 intensification of the Pacific Walker circulation, and the enhanced deep convection
429 and a stronger upward motion over the TWP which could extend to the upper
430 troposphere.

431 **3.3 Implications for the concentrations of water vapor and CO in the TTL**
432 **and lower stratosphere**

433 Previous studies showed that the enhanced deep convection and upward motion
434 could lead to increased CO in the UTLS (e.g., Duncan et al., 2007; Livesey et al.,
435 2013). At the same time, water vapor mixing ratios in the UTLS may increase due to
436 the enhanced upward motion which could bring more wet air from low altitude to
437 high altitude (e.g., Rosenlof, 2003; Lu et al., 2020). However, the water vapor mixing
438 ratios in the lower stratosphere also depend on the tropopause temperature (e.g.,
439 Highwood and Hoskins, 1998; Garfinkel et al., 2018; Pan et al., 2019). Hence, the
440 relationship between the intensity of upward motion and the water vapor
441 concentration in the UTLS is complex. Here, the relationship between the trends of
442 the upward motion over the TWP and the changes in CO and water vapor in the ULTS
443 simulated with WACCM4 are analyzed.

444 The trends of CPTT, the 100 hPa streamfunction, and the water vapor
445 concentration are shown based on the Control and the Fixsst simulation as well as
446 their difference in Figs. 7d-i. The changes in the deep convection could lead to the
447 changes in the atmospheric circulation by releasing the latent heat. The changes in the
448 tropical deep convection lead to a Rossby-Kelvin wave response at the UTLS level
449 and then induce the changes in the air temperature near the tropopause (e.g., Gill,
450 1980; Highwood and Hoskins, 1998). The trends of the 100 hPa streamfunction show
451 a Rossby wave response over the TWP and a Kelvin wave response over the tropical
452 eastern Pacific in the Control simulation (Fig. 7d), which is caused by the changes in
453 the deep convection over the tropical Pacific. The Rossby-Kelvin wave response
454 further leads to the decrease the CPTT over the TWP and the increase of the CPTT

455 over the tropical eastern Pacific. Previous studies suggest that the lower stratospheric
456 water vapor is mainly influenced by the coldest temperature near the tropopause (e.g.,
457 Garfinkel et al., 2018; Zhou et al., 2021). Since the TWP has the coldest CPTT in the
458 boreal winter (e.g., Pan et al., 2016), the significantly decreased CPTT over the TWP
459 may result in significantly dried lower stratosphere (Fig. 7g). The intensity of the
460 upward motion over the TWP shows negative correlations with the concentration of
461 the tropical lower stratospheric water vapor (not shown). Hence, the enhanced upward
462 motion over the TWP may correspond to a dried lower stratosphere. The CPTT shows
463 weak trends over the TWP, and the tropical water vapor shows insignificant trends at
464 70 hPa in the Fixsst simulation. The comparison between the Control simulation and
465 the Fixsst simulation suggests that the trends of the deep convection, the CPTT, and
466 the lower stratospheric water vapor concentration in the tropics in NDJFM during
467 1958-2017 are dominated by the trends of the global SSTs, while other external
468 forcings may play minor roles.

469 Generally, the intensified upward motion may lead to more tropospheric trace
470 gases lifting to the upper troposphere and entering the lower stratosphere (e.g.,
471 Rosenlof, 2003; Lu et al., 2020). Here we use CO as a tropospheric tracer to detect the
472 possible influences of the enhanced upward motion over the TWP on the
473 transportation of the tropospheric trace gases to the upper troposphere and the lower
474 stratosphere. Due to the data limitation, it is not possible to show the corresponding
475 changes of trace gases by observations in NDJFM during 1958-2017. Here, the trends
476 of CO at around 200 hPa from MOPITT and MLS observations are shown in the Fig.

477 8. The CO increased significantly over the TWP in NDJFM in the upper troposphere
478 from the MOPITT (at 200 hPa during 2000-2017) and MLS data (at 215 hPa during
479 2005-2017). The concentration of MLS CO over the TWP is approximately 80 ppbv
480 at 215 hPa from MLS observations and 70 ppbv at 200 hPa from MOPITT
481 observations, which is consistent with previous study (e.g., Huang et al., 2016). The
482 MLS CO data show that the area-averaged CO increased approximately 2.0 ± 3.7 ppbv
483 decade⁻¹ over the TWP in NDJFM during 2005-2017. The area-averaged MOPITT CO
484 data show a stronger increase of approximately 5.0 ± 3.1 ppbv decade⁻¹ at 200 hPa
485 from 2000 to 2017 (significant at the 95% confidence level). It should be pointed out
486 that the linear trends of CO are calculated based on the satellite data which only cover
487 14 or 18 years due to the data limitation. Hence, the linear trends of CO may have
488 uncertainties particularly in the regions with large interannual variations. To partially
489 overcome this shortage, the trends of MLS CO at 215 hPa during time periods of
490 2005-2016, 2006-2016, 2006-2017, and 2007-2016 and the trends of MOPITT CO at
491 200 hPa during time periods of 2000-2016, 2001-2016, 2001-2017, and 2002-2016
492 are shown in Supplementary Fig. 6. It could be found that the CO in the upper
493 troposphere increased robustly over the TWP from both the MLS and MOPITT data.
494 Overall, though the observed CO only covers less than 20 years, the results from the
495 satellite data suggest a possible impact of the intensified upward motion over the
496 TWP on the trace gases in the upper troposphere.

497 To further illustrate the impacts of the enhanced upward motion on the trace gas
498 in the upper troposphere and lower stratosphere, the Control and Fixsst simulations

499 with WACCM4 are used. The trends of the CO concentrations from the Control and
500 Fixsst simulations as well as their differences are shown in Fig. 9. The tropical CO at
501 150 hPa shows significantly increasing trends both in the Control and the Fixsst
502 simulations at rates of $3.4 \text{ ppbv decade}^{-1}$ and $3.2 \text{ ppbv decade}^{-1}$, respectively, (Figs. 9a
503 and b). This suggests that the surface emission of the CO exerts the most important
504 effect on the increase of the tropical CO concentration. The differences of the CO
505 trends at 150 hPa between the Control simulation and the Fixsst simulation are also
506 displayed in Fig. 9c. Since the surface emission inventories of the two simulations are
507 the same, it can be inferred that the trends of the CO concentration in Fig. 9c are
508 mainly caused by the changes in the atmospheric circulation induced by the changes
509 in the global SSTs. The difference of the CO concentration at 150 hPa between the
510 Control simulation and the Fixsst simulation shows a significantly increasing trend at
511 a rate of $0.2 \pm 0.1 \text{ ppbv decade}^{-1}$ over the TWP (significant at the 95% confidence
512 level). At the same time, decreasing trends over the central Africa exist, which
513 resembles to the trend patterns of the vertical velocity in the lower TTL and the deep
514 convection (Figs. 5i and 7c). This indicates that the enhanced deep convection in the
515 TWP lead to the strengthened upward motion over the TWP, which results in an extra
516 6% increasing trend of CO in the upper troposphere over the TWP. It could also be
517 found that CO also increased in the mid latitudes of the southern hemisphere (Fig. 9c).
518 According to previous studies, the CO perturbation from the Indonesian fires at upper
519 troposphere could be transported to the tropical Indian Ocean by easterly winds and
520 then to the subtropics in the southern hemisphere through the southward flow during

521 boreal winter. The CO perturbation then spreads rapidly circling the globe following
522 the subtropical jet (Duncan et al., 2007). This is consistent with our results which
523 show intensified northerlies over the subtropical Indian Ocean (15°S-25°S,
524 60°E-100°E) at a rate of approximately $0.2 \text{ m s}^{-1} \text{ decade}^{-1}$ and strengthened westerlies
525 over the subtropical Indian Ocean and western Pacific (20°N-35°N, 60°E-160°E) at a
526 rate of approximately $0.3 \text{ m s}^{-1} \text{ decade}^{-1}$ (Figs. 5c and f).

527 The trends of the zonal mean CO concentration from model simulations are
528 displayed in Figs. 10a-c. The zonal mean CO shows significantly increasing trends at
529 all levels in the Control simulation and the Fixsst simulation, while the difference of
530 the zonal mean CO between the Control simulation and the Fixsst simulation shows
531 significantly increasing trends in the TTL but negative trends in the middle
532 troposphere in the tropics and the Northern Hemisphere. At the same time, the
533 difference of CO concentration between the Control simulation and the Fixsst
534 simulation averaged in the western Pacific (100°E-180°E) shows significantly
535 increasing trends in the tropics (20°S-10°N) from the surface to the TTL (Fig. 10f).
536 The CO in the layer 150-70 hPa over the TWP increased $3.2 \text{ ppbv decade}^{-1}$ and 2.8
537 ppbv decade^{-1} in the Control and Fixsst simulations in NDJFM during 1958-2017,
538 respectively. And the CO difference between the Control and Fixsst simulations
539 increased $0.4 \pm 0.2 \text{ ppbv decade}^{-1}$ (significant at the 95% confidence level) in the layer
540 150-70 hPa over the TWP, which suggests that the intensifying upward motion over
541 the TWP and the tropical upwelling of BDC could lead to an extra 14% increasing
542 trend of CO. This indicates that the increased zonal mean CO in the TTL (Fig. 10c) is

543 mainly transported through the western Pacific bands and highlights the importance of
544 the upward motion over the TWP in elevating trace gases from the surface to the
545 upper troposphere.

546 To understand the CO trends in the Control and Fixsst simulations and their
547 differences, the trends of vertical velocity averaged over the globe and the TWP band
548 are given in Fig. 11. The zonal mean w shows weak and even decreasing trends in the
549 tropics while the w over the TWP intensified in the Control simulation in NDJFM
550 during 1958-2017. This is consistent with Fig. 5. While the SSTs fixed to
551 climatological values, the zonal mean w shows weak trends and the w over the TWP
552 shows significantly negative trends. The changes in the global SSTs therefore leads to
553 the increase of the w over the TWP region as indicated in the differences between the
554 two simulations in Fig. 11f. In summary, the CO shows increasing trends (3.5 ppbv
555 decade⁻¹) at 150 hPa over the TWP in NDJFM during 1958-2017 induced by the
556 changes in the surface emissions and the upward motion. The trends of CO at 150 hPa
557 over the TWP in NDJFM during 1958-2017 in the Fixsst simulation mainly include
558 the impact induced by the increased surface emissions since the upward motion over
559 the TWP in the Fixsst simulation shows weak trends. The difference between the
560 Control and Fixsst simulations indicates that the enhanced tropospheric upward
561 motion over the TWP forced by the changes in the global SSTs leads to some extra
562 increase of CO concentrations in the upper troposphere. It should be mentioned that
563 the increasing trends of CO in the lower troposphere in Fig. 10f may be mainly caused
564 by the changes in the horizontal winds. Girach and Nair (2014) suggested that

565 enhanced deep convection and the subsequent intensified upward motion may lead to
566 a decreased CO concentration in the lower troposphere and an increased CO
567 concentration in the upper troposphere. The trends of horizontal winds at 925 hPa are
568 shown in Supplementary Fig. 8c. There are northerly trends over east Asia and
569 northeasterly trends near the south Asia (Supplementary Fig. 8c), which suggests that
570 more CO-rich air from east Asia and south Asia could be transported to the TWP in
571 the Control simulation comparing to the Fixsst simulation. Since the CO
572 concentration in the lower troposphere over the northern Pacific is higher than that
573 over southern Pacific, the northerly trends over the western and central Pacific may
574 also contribute to the increased CO in the lower troposphere over the TWP in Fig. 10f.

575 As discussed in the Introduction, the tropospheric trace gases enter the
576 stratosphere mainly through the large-scale tropical upwelling associated with the BD
577 circulation. The trends of the BD circulation in different model simulations as well as
578 their differences are displayed in Fig. 12. The tropical upwelling of BDC (w^*)
579 calculated using the TEM formula increased significantly in the lower stratosphere
580 over past decades as seen in the JRA55 data and the Control simulation (Figs. 12a and
581 12b). We found that the 70 hPa upward mass flux in NDJFM in the tropics
582 (15°S - 15°N) increased $2.8 \pm 1.9\%$ decade⁻¹ (significant at the 95% confidence level) in
583 the JRA55 data from 1958 to 2017 (Fig. 12a) and $4.6 \pm 4.3\%$ decade⁻¹ (significant at
584 the 95% confidence level) in the MERRA2 data from 1980 to 2017 (Supplementary
585 Fig. 7b). From the ERA5 data, the 70 hPa upward mass flux in NDJFM increased in
586 the north hemisphere (0 - 15°N) at a rate of $5.0 \pm 2.8\%$ decade⁻¹ (significant at the 95%

587 confidence level), but decreased significantly in the south hemisphere (0-15°S) during
588 1958-2017 (Supplementary Fig. 7a). On average, the trend of the 70 hPa upward mass
589 flux in NDJFM in the tropics (15°S-15°N) is not significant in ERA5. In fact, many
590 previous studies have investigated the trends of BDC. For example, Abalos et al.
591 (2015) investigated the trends of BDC derived from JRA55, MERRA, and
592 ERA-Interim data during 1979-2012 and suggested that the BDC in JRA55 and
593 MERRA significantly strengthened throughout the layer 100-10 hPa with a rate of
594 2-5% decade⁻¹, while the BDC in ERA-Interim shows weakening trends. Diallo et al.
595 (2021) compared the trends of the BDC in the ERA5 and ERA-Interim during
596 1979-2018 and pointed out that the BDC in the ERA-Interim shows weakening trend
597 and the BDC in the ERA5 strengthened at a rate of 1.5% decade⁻¹ which is more
598 consistent with other studies. In the present study, we only focus on the trend of the
599 BDC in the wintertime (NDJFM) in the tropics (15°S-15°N) during 1958-2017, which
600 may lead to some differences between our result and that in the previous studies.
601 Overall, the trends of the tropical upwelling of BDC derived from JRA55, MERRA2
602 data and the Control simulation are similar to that in previous studies using both
603 reanalysis datasets and model results (e.g., Butchart et al., 2010; Abalos et al., 2015;
604 Fu et al., 2019; Rao et al., 2019; Diallo et al., 2021). However, the tropical upwelling
605 of the BDC decreased in ERA5 data in the tropics (15°S-15°N), which are different
606 from the results in JRA55 and MERRA2.

607 In the Fixsst simulation, the trend of w^* is much weaker and not significant in
608 most areas. The changes in the global SSTs therefore play an important role in the

609 intensification of the shallow branch of the BDC as shown by the differences between
610 the two simulations in Fig. 12d. In summary, the tropical upwelling of the BDC is
611 likely strengthened as shown in JRA55 and MERRA2 reanalyses as well as model
612 simulations, although there are some uncertainties since the ERA5 data show a
613 negative trend. This may impact on the transport of the tropospheric trace gases from
614 the TTL to a higher altitude. The increased concentration of CO in the UTLS in Fig.
615 9c and 10f may be due to a combined effect of the strengthened tropical upwelling of
616 the BD circulation and the enhanced upward motion over the TWP. The enhancement
617 of upward motion over the TWP, which transported more tropospheric trace gases to
618 the upper troposphere, works together with the strengthened BD circulation under
619 global warming may lead to an increase of tropospheric trace gases over the TWP in
620 the lower stratosphere.

621 **4 Summary and Discussion**

622 The recent trends of the upward motion from the lower to the upper troposphere
623 in boreal winter over the TWP is investigated for the first time based on the JRA55,
624 ERA5, MERRA2 datasets and four WACCM4 simulations ([Table 2](#)). The upward
625 motion at 150 hPa over the TWP in NDJFM increased $8\pm 3.1\%$ decade⁻¹ and $3.6\pm 3.3\%$
626 decade⁻¹ in NDJFM from 1958 to 2017 in JRA55 and ERA5 reanalysis datasets,
627 respectively ([Table 3](#)). Despite the possible discontinuities between the radiosonde era
628 (after 1958) and the satellite era (after 1979), the upward motion at 150 hPa over the
629 TWP in NDJFM increased $7.5\pm 7.1\%$ decade⁻¹ during 1980-2017 in MERRA2 data.
630 Such intensification of the upward motion over the TWP also exist in the middle and

631 | lower_troposphere in NDJFM in JRA55, ERA5, and MERRA2, which can be
632 | confirmed by the WACCM4 model simulations. Comparing the results between the
633 | Control and Fixsst simulations with WACCM4, it is found that the trend of the
634 | upward motion over the TWP is closely related to the changes in global SSTs,
635 | especially the SST warming over the eastern maritime continent and tropical western
636 | Pacific (see the results from the experiments R1 and R2 in Fig. 7). Warmer SSTs over
637 | the eastern maritime continent and tropical western Pacific (approximately 0.5 K) lead
638 | to a strengthened Pacific Walker circulation, enhanced deep convection and
639 | approximately 27% intensified upward motion at 150 hPa over the TWP as shown by
640 | the results from the experiments R1 and R2. The enhanced deep convection over the
641 | TWP could lead to a dryer lower stratosphere over the TWP, as the strong upward
642 | motion and the Rossby-Kelvin wave responses induce a colder tropopause over the
643 | TWP. It should be pointed out that the results in the present study are mainly based on
644 | the reanalyses data, and some uncertainties may exist. The availability of more high
645 | resolution observations in the future may enhance the quality of the reanalysis data.

646 | Results from the Control simulation indicate that the CO concentrations
647 | increased significantly from the surface to the stratosphere over the TWP. The CO at
648 | 150 hPa increased at a rate of approximately 3.4 ppbv decade⁻¹ with increased surface
649 | emissions and the enhanced upward motion over the TWP. Specifically, an
650 | enhancement of tropospheric upward motion and subsequent upward transport of
651 | trace gases over the TWP lead to an extra 6% increasing trend of CO concentrations
652 | in the upper troposphere.

653 Furthermore, the upward mass fluxes at 70 hPa in the tropics (15°S-15°N) show
654 strengthening trends at rates of $2.8 \pm 1.9\%$ decade⁻¹ and $4.6 \pm 4.3\%$ decade⁻¹ in JRA55
655 data (during 1958-2017) and MERRA2 data (during 1980-2017) in NDJFM,
656 respectively, which is consistent with previous studies (e.g., Butchart et al., 2010; Fu
657 et al., 2019; Rao et al., 2019). However, such enhancement in tropical upward mass
658 flux at 70 hPa has large uncertainties since the ERA5 data show a negative and
659 insignificant trend (Supplementary Fig. 7a). The results from the Control and Fixsst
660 simulations indicate that the elevated CO in the upper troposphere is further uplifted
661 to the lower stratosphere by the intensified tropical upwelling of the BD circulation
662 due mainly to global SST warming and lead to an increase of CO in the lower
663 stratosphere. An extra 14% increasing trend of CO at the layer 150-70 hPa over the
664 TWP is derived from the Control and Fixsst simulations.

665 Tropospheric trace gases and aerosols have important impacts on the
666 stratospheric processes if they enter the stratosphere. For example, ozone-depleting
667 substances, CH₄ and N₂O could influence on the stratospheric ozone significantly
668 (e.g., Shindell et al., 2013; Wang et al., 2014; WMO, 2018), which also modify the
669 temperature in the stratosphere significantly through their strong radiative effects.
670 Water vapor in the lower stratosphere, in particular, has a significant warming effect
671 on the surface climate (Solomon et al., 2010). Therefore, changes of trace gases in the
672 UTLS have important impacts on both tropospheric and stratospheric climate. Our
673 results suggest that the upward motion over the TWP and the vertical component of
674 the BDC at the lower stratosphere level have been intensified. These results suggest

675 that the emission from the maritime continent and surrounding areas may play a more
676 important role in the stratospheric processes and the global climate. In addition, more
677 very short lived substances emitted from the tropical ocean could be elevated to the
678 TTL by the enhanced convection and then transported into the stratosphere by the
679 large-scale uplifts and exert important effects on the stratospheric chemistry. However,
680 the quantitative impacts of the intensified upward motion over the TWP on
681 tropospheric and stratospheric trace gases and aerosols and their climate feedbacks
682 await further investigation using more observations and model simulations.

683

684 **Competing interests.** The authors declare that they have no conflict of interest.

685

686 **Author contributions.** KQ ran the models and wrote the first draft. WW provided
687 suggestions about the statistical methods and model simulations. WT designed the
688 study. RH, MX, and TW contributed to the manuscript writing. YP provided the data
689 used in the study. All authors contributed to the improvement of the results.

690

691

692 **Acknowledgements.** This research is supported by Strategic Priority Research
693 Program of Chinese Academy of Sciences (XDA17010106), the National Natural
694 Science Foundation of China (42075055) and the Supercomputing Center of Lanzhou
695 University.

696 The authors gratefully acknowledge the data used in the present study provided by the
697 corresponding scientific groups. The JRA55 data are from:

698 <http://rda.ucar.edu/datasets/ds628.0/>.

699 The SST data is obtained from HadISST:
700 <https://www.metoffice.gov.uk/hadobs/hadisst/data/download.html>.
701 The ERA5 data and ERA5.1 data are extracted from:
702 <https://cds.climate.copernicus.eu/#!/search?text=ERA5&type=dataset>.
703 The MERRA2 data are downloaded from:
704 <https://search.earthdata.nasa.gov/search?q=MERRA2&fst0=Atmosphere>.
705 The OLR data are from https://psl.noaa.gov/data/gridded/data.interp_OLR.html.

706

707 **References:**

- 708 Abalos, M., Legras, B., Ploeger, F., and Randel, W. J.: Evaluating the advective
709 Brewer-Dobson circulation in three reanalyses for the period 1979-2012, *J.*
710 *Geophys. Res.*, 120,7534-7554, doi:10.1002/2015JD023182, 2015.
- 711 Andrews, D. G., and McIntyre, M. E.: Planetary waves in horizontal and vertical shear:
712 the generalized Eliassen-Palm relation and the mean zonal acceleration, *J. Atmos.*
713 *Sci.*, 33, 2031 – 2048, 1976
- 714 Ashfold, M. J., Pyle, J. A., Robinson, A. D., Meneguz, E., Nadzir, M. S. M., Phang, S.
715 M., Samah, A. A., Ong, S., Ung, H. E., Peng, L. K., Yong, S. E., and Harris, N. R.
716 P.: Rapid transport of East Asian pollution to the deep tropics, *Atmos. Chem.*
717 *Phys.*, 15, 3565-3573, doi:10.5194/acp-15-3565-2015, 2015.
- 718 Bergman, J. W., Jensen, E. J., Pfister, L., and Yang, Q.: Seasonal differences of
719 vertical-transport efficiency in the tropical tropopause layer: On the interplay
720 between tropical deep convection, large-scale vertical ascent, and horizontal
721 circulations, *J. Geophys. Res.*, 117, D05302, doi:10.1029/2011JD016992, 2012.
- 722 Brewer, A. M.: Evidence for a world circulation provides by the measurements of
723 helium and water vapor distribution in the stratosphere, *Q. J. R. Meteorol. Soc.*,
724 75, 351–363, 1949.
- 725 Butchart, N., Cionni, I., Eyring, V., Shepherd, T. G., Waugh, D. W., Akiyoshi, H.,
726 Austin, J., Brühl, C., Chipperfield, M. P., Cordero, E., Dameris, M., Deckert, R.,

727 Dhomse, S., Frith, S. M., Garcia, R. R., Gettelman, A., Giorgetta, M. A.,
728 Kinnison, D. E., Li, F., Mancini, E., McLandress, C., Pawson, S., Pitari, G.,
729 Plummer, D. A., Rozanov, E., Sassi, F., Scinocca, J. F., Shibata, K., Steil, B., and
730 Tian, W.: Chemistry–Climate Model simulations of twenty-first century
731 stratospheric climate and circulation changes, *J. Climate*, 23, 5349–5374,
732 <https://doi.org/10.1175/2010JCLI3404.1>, 2010.

733 Cane, M. A., Clement, A. C., Kaplan, A., Kushnir, Y., Pozdnyakov, D., and Seager, R.,
734 et al.: Twentieth-century sea surface temperature trends, *Science*, 275(5302),
735 957-960, DOI: 10.1126/science.275.5302.957, 1997.

736 Deeter, M. N., Edwards, D. P., Francis, G. L., Gille, J. C., Mao, D., Martinez-Alonso,
737 S., Worden, H. M., Ziskin, D., and Andreae, M. O.: Radiance-based retrieval bias
738 mitigation for the MOPITT instrument: the version 8 product, *Atmos. Meas.*
739 *Tech.*, 12, 4561–4580, <https://doi.org/10.5194/amt-12-4561-2019>, 2019.

740 Deser, C., Phillips, A. S., and Alexander, M. A.: Twentieth century tropical sea surface
741 temperature trends revisited, *Geophys. Res. Lett.*, 37(10), L10701,
742 doi:10.1029/2010GL043321, 2010.

743 Diallo, M., Ern, M., and Ploeger, F.: The advective Brewer – Dobson circulation in
744 the ERA5 reanalysis: climatology, variability, and trends, *Atmos. Chem. Phys.*,
745 21, 7515 – 7544, <https://doi.org/10.5194/acp-21-7515-2021>, 2021.

746 Dobson G. M. B.: Origin and distribution of the polyatomic molecules in the
747 atmosphere, *Proc. R. Soc. Lond. Ser. A*. 236: 187-193, 1956.

748 Duncan, B. N., Logan J. A., Bey, I., Megretskaia, I. A., Yantosca, R. M., Novelli, P. C.,
749 Jones, N. B. and Rinsland, C. P.: Global budget of CO, 1988-1997: Source
750 estimates and validation with a global model, *J. Geophys. Res.*, 112, D22301,
751 doi:10.1029/2007JD008459, 2007.

752 Feng, W., Chipperfield, M. P., Dorf, M., Pfeilsticker, K., and Ricaud, P.: Mid-latitude
753 ozone changes: studies with a 3-D CTM forced by ERA-40 analyses, *Atmos.*
754 *Chem. Phys.*, 7, 2357 – 2369, doi:10.5194/acp-7-2357-2007, 2007.

755 Fu, Q., Solomon, S., Pahlavan, H. A., and Lin, P.: Observed changes in
756 Brewer–Dobson circulation for 1980–2018, *Environ. Res. Lett.*, 14, 114 026,

757 <https://doi.org/10.1088/1748-9326/ab4de7>, 2019.

758 Fueglistaler, S., Desller, A. E., Dunkerton, T. J., Folkins, I., Fu, Q., and Mote P.:
759 Tropical tropopause layer, *Rev. Geophys.*, 47(1), RG1004,
760 doi:10.1029/2008RG000267, 2009.

761 Fueglistaler, S., Wernli, H., and Peter, T.: Tropical troposphere-to-stratosphere
762 transport inferred from trajectory calculations, *J. Geophys. Res.*, 109, D03108,
763 doi:10.1029/2003JD004069, 2004.

764 Fujiwara, M., Wright, J. S., Manney, G. L., Gray, L. J., Anstey, J., Birner, T., Davis, S.,
765 Gerber, E. P., Harvey, V. L., Hegglin, M. I., Homeyer, C. R., Knox, J. A., Krüger,
766 K., Lambert, A., Long, C. S., Martineau, P., Molod, A., Monge-Sanz, B. M.,
767 Santee, M. L., Tegtmeier, S., Chabrillat, S., Tan, D. G. H., Jackson, D. R.,
768 Polavarapu, S., Compo, G. P., Dragani, R., Ebisuzaki, W., Harada, Y., Kobayashi,
769 C., McCarty, W., Onogi, K., Pawson, S., Simmons, A., Wargan, K., Whitaker, J.
770 S., and Zou, C.-Z.: Introduction to the SPARC Reanalysis Intercomparison
771 Project (S-RIP) and overview of the reanalysis systems, *Atmos. Chem. Phys.*, 17,
772 1417-1452, <https://doi.org/10.5194/acp-17-1417-2017>, 2017

773 Garfinkel, C. I., Waugh, D. W., and Polvani, L. M.: Recent Hadley cell expansion:
774 The role of internal atmospheric variability in reconciling modeled and observed
775 trends, *Geophys. Res. Lett.*, 42(24), 10824-10831,
776 <https://doi.org/10.1002/2015GL066942>, 2015

777 Garfinkel, C. I., Waugh, D. W., Oman, L. D., Wang, L., and Hurwitz, M. M.:
778 Temperature trends in the tropical upper troposphere and lower stratosphere:
779 Connections with sea surface temperatures and implications for water vapor and
780 ozone, *J. Geophys. Res.*, 118, 9658-9672, doi:10.1002/jgrd.50772, 2013.

781 Garfinkel, C. O., Gordon, A., Oman, L. D., Li, F., Davis, S., and Pawson, S.:
782 Nonlinear response of tropical lower-stratospheric temperature and water vapor
783 to ENSO, *Atmos. Chem. Phys.*, 18, 4597-4615,
784 <https://doi.org/10.5194/acp-18-4597-2018>, 2018.

785 Gelaro, R., Mccarty, W., and Suárez, M. J.: The modern-era retrospective analysis for
786 research and applications, version 2 (merra-2), *J. Climate*, 30(14), 5419-5454,

787 <https://doi.org/10.1175/JCLI-D-16-0758.1>, 2017

788 Gettelman, A., Holton, J. R., and Douglass, A. R.: Simulations of water vapor in the
789 lower stratosphere and upper troposphere, *J. Geophys. Res.*, 105(D7), 9003-9023,
790 <https://doi.org/10.1029/1999JD901133>, 2000.

791 Gill, A. E.: Some simple solutions for heat-induced tropical circulation, *Q. J. R.*
792 *Meteorolog. Soc.*, 106, 447-462, doi:10.1002/qj.49710644905, 1980.

793 Girach, I. A., and Nair, P. R.: Carbon monoxide over Indian region as observed by
794 MOPITT, *Atmos. Environ.*, 99, 599-609,
795 <http://dx.doi.org/10.1016/j.atmosenv.2014.10.019>, 2014.

796 Haines, P. E., and Esler, J. G.: Determination of the source regions for surface to
797 stratosphere transport: An Eulerian backtracking approach, *Geophys. Res. Lett.*,
798 41, 1343-1349, doi:10.1002/2013GL058757, 2014.

799 Harada, Y., Kamahori, H., Kobayashi, C., Endo, H., Kobayashi, S., Ota, Y., Onoda, H.,
800 Onogi, K., Miyaoka, K., and Takahashi, K.: The JRA-55 Reanalysis:
801 Representation of atmospheric circulation and climate variability, *J. Meteorol.*
802 *Soc. Jpn.*, 94(3), 269-302, <https://doi.org/10.2151/jmsj.2016-015>, 2016.

803 Hersbach, H., Bell, B., Berrisford, P., Hirahara, S., Horányi, A., Muñoz-Sabater, J.,
804 and Nicolas, J., et al.: The ERA5 global reanalysis, *Q. J. R. Meteorol. Soc.*, 146,
805 1999-2049, DOI: 10.1002/qj.3803, 2020.

806 Highwood, E. J., and Hoskins, B. J.: The tropical tropopause, *Q. J. R. Meteorol. Soc.*,
807 124(549), 1579-1604, DOI: 10.1002/qj.49712454911, 1998.

808 Hitchcock, P.: On the value of reanalysis prior to 1979 for dynamical studies of
809 stratosphere-troposphere coupling, *Atmos. Chem. Phys.*, 19, 2749-2764,
810 <https://doi.org/10.5194/acp-19-2749-2019>, 2019

811 Holton, J. R., Haynes, P. H., McIntyre, M. E., Douglass, A. R., Rood, R. B., and
812 Pfister, L.: Stratosphere-troposphere exchange, *Rev. Geophys.*, 33,
813 403-439, <https://doi.org/10.1029/95RG02097>, 1995.

814 Hosking, J. S., Russo, M. R., Braesicke, P., and Pyle, J. A.: Tropical convective
815 transport and the Walker circulation, *Atmos. Chem. Phys.*, 12, 9791-9797,
816 doi:10.5194/acp-12-9791-2012, 2012

817 Hu, D., Guan, Z., Tian, W., and Ren, R.: Recent strengthening of the stratospheric
818 Arctic vortex response to warming in the central North Pacific, 9, 1697,
819 <https://doi.org/10.1038/s41467-018-04138-3>, 2018.

820 Hu, D., Guo, Y., Wang, F., Xu, Q., Li, Y., Sang, W., Wang, X., and Liu, M.:
821 Brewer-Dobson circulation: Recent-Past and near-future trends simulated by
822 chemistry-climate models, *Adv. Meteorol.*, 2017, 1-13,
823 <https://doi.org/10.1155/2017/2913895>, 2017.

824 Hu, D., Tian, W., Guan, Z., Guo, Y., and Dhomse, S.: Longitudinal asymmetric trends
825 of tropical cold-point tropopause temperature and their link to strengthened
826 Walker circulation, *J. Climate*, 29(21), 7755–7771,
827 <https://doi.org/10.1175/JCLI-D-15-0851.1>, 2016.

828 Hu, P., Huangfu, J., Chen, W., and Huang, R.: Impacts of early/late South China Sea
829 summer monsoon withdrawal on tropical cyclone genesis over the western North
830 Pacific, *Clim. Dynam.*, 55(19), 1507-1520,
831 <https://doi.org/10.1007/s00382-020-05339-7>, 2020.

832 Huang, L., Jiang, J. H., Murray, L. T., Damon, M. R., Su, H., and Livesey, N.:
833 Evaluation of UTLS carbon monoxide simulations in GMI and GEOS-Chem
834 chemical transport models using Aura MLS observations, *Atmos. Chem. Phys.*,
835 16, 5641-5663, doi:10.5194/acp-16-5641-2016, 2016.

836 Krüger, K., Tegtmeier, S., and Rex, M.: Long-term climatology of air mass transport
837 through the Tropical Tropopause Layer (TTL) during NH winter, *Atmos. Chem.*
838 *Phys.*, 8, 813–823, doi:10.5194/acpd-7-13989-2007, 2008.

839 L’Heureux, M. L., Lee, S., and Lyon, B.: Recent multidecadal strengthening of the
840 Walker circulation across the tropical Pacific, *Nat. Clim. Change*, 3, 571–576,
841 doi: 10.1038/nclimate1840, 2013.

842 Levine, J. G., Braesicke, P., Harris, N. R. P., Pyle, J. A.: Seasonal and inter-annual
843 variations in troposphere-to-stratosphere transport from the tropical tropopause
844 layer, *Atmos. Chem. Phys.*, 8, 3689-3703, DOI:10.5194/acpd-8-489-2008, 2008.

845 Levine, J. G., Braesicke, P., Harris, N. R. P., Savage, N. H., and Pyle, J. A.: Pathways
846 and timescales for troposphere-to-stratosphere transport via the tropical

847 tropopause layer and their relevance for very short lived substances, *J. Geophys.*
848 *Res.*, 112, D04308, doi:10.1029/2005JD006940, 2007.

849 Liebmann, B., and Smith, C. A.: Description of a complete (interpolated) outgoing
850 longwave radiation dataset, *B. Am. Meteorol. Soc.*, 77, 1275-1277, doi:
851 10.1175/1520-0477(1996)077<1255:EA>2.0.CO;2, 1996.

852 Livesey, N. J., Logan, J. A., Santee, M. L., Waters, J. W., Doherty, R. M., Read, W. G.,
853 Froidevaux, L., and Jiang, J. H.: Interrelated variations of O₃, CO and deep
854 convection in the tropical/subtropical upper troposphere observed by the Aura
855 Microwave Limb Sounder (MLS) during 2004-2011, *Atmos. Chem. Phys.*, 13,
856 579-598, doi:10.5194/acp-13-579-2013, 2013.

857 Livesey, N. J., Read, W. G., Wagner, P. A., Froidevaux, L., Lambert, A., Manney, G. L.,
858 Millán, L., Pumphrey, H. C., Santee, M. L., Schwartz, M. J., Wang, S., Fuller, R.
859 A., Jarnot, R. F., Knosp, B. W., and Martinez, E.: EOS MLS Version 4.2x Level
860 2 data quality and description document, Jet Propulsion Laboratory, California
861 Institute of Technology, Pasadena, CA, 2015.

862 Lin, P., Ming, Y., and Ramaswamy, V.: Tropical climate change control of the lower
863 stratospheric circulation, *Geophys. Res. Lett.*, 42(3), 941-948, doi:
864 10.1002/2014GL062823, 2015.

865 Logan, J. A., Megretskaya, I. A., Nassar, R., Murray, L. T., Zhang, L., Bowman, K. W.,
866 Worden, H. M., and Luo, M.: Effects of the 2006 El Niño on tropospheric
867 composition as revealed by data from the Tropospheric Emission Spectrometer
868 (TES), *Geophys. Res. Lett.*, 35, L03816,
869 <https://doi.org/10.1029/2007GL031698>, 2008.

870 Long, C. S., Fujiwara, M., Davis, S., Mitchell, D. M., and Wright, C. J.: Climatology
871 and interannual variability of dynamic variables in multiple reanalyses evaluated
872 by the SPARC Reanalysis Intercomparison Project (S-RIP), *Atmos. Chem. Phys.*,
873 17, 14593-14629, <https://doi.org/10.5194/acp-17-14593-2017>, 2017.

874 Lu, J., Vecchi, G. A., and Reichler, T.: Expansion of the Hadley cell under global
875 warming, *Geophys. Res. Lett.*, 34(6), L06805, doi:10.1029/2006GL028443,
876 2007

877 Lu, J., Xie, F., Sun, C., Luo, J., Cai, Q., Zhang, J., Li, J., and Tian, H.: Analysis of
878 factors influencing tropical lower stratospheric water vapor during 1980–2017,
879 *npj Clim. Atmos. Sci.*, 3(1), 35, <https://doi.org/10.1038/s41612-020-00138-7>,
880 2020.

881 Ma, S., and Zhou, T.: Robust Strengthening and Westward Shift of the Tropical
882 Pacific Walker Circulation during 1979–2012: A Comparison of 7 Sets of
883 Reanalysis Data and 26 CMIP5 Models, *J. Climate*, 29, 3097–3118, doi:
884 10.1175/JCLI-D-15-0398.1, 2016.

885 Marsh, D. R., Mills, M. J., Kinnison, D. E., Lamarque, J., Calvo, N., and Polvani, L.
886 M.: Climate change from 1850 to 2005 simulated in CESM1 (WACCM), *J.*
887 *Climate*, 26, 7372–7391, <https://doi.org/10.1175/JCLI-D-12-00558.1>, 2013.

888 McGregor, S., Timmermann, A., Stuecker, M. F., England, M. H., Merrifield, M., Jin,
889 F., and Chikamoto, Y.: Recent Walker circulation strengthening and Pacific
890 cooling amplified by Atlantic warming, *Nat. Clim. Change*, 4, 888–882,
891 <https://doi.org/10.1038/nclimate2330>, 2014.

892 Meng, Q., Latif, M., Park, W., Keenlyside, N. S., Semenov, V. A., and Martin, T.:
893 Twentieth century Walker circulation change: Data analysis and model
894 experiments, *Clim. Dynam.*, 38, 1757–1773,
895 <https://doi.org/10.1007/s00382-011-1047-8>, 2012.

896 Minganti, D., Chabrillat, S., Christophe, Y., Errera, Q., Abalos, M., Prignon, M.,
897 Kinnison, D. E., and Mahieu, E.: Climatological impact of the Brewer–Dobson
898 circulation on the N₂O budget in WACCM, a chemical reanalysis and a CTM
899 driven by four dynamical reanalyses, *Atmos. Chem. Phys.*, 20, 12609–12631,
900 <https://doi.org/10.5194/acp-20-12609-2020>, 2020.

901 Navarro, M. A., Atlas, E. L., Saiz-Lopez, A., Rodriguez-Lloveras, X., Kinnison, D. E.,
902 Lamarque, J., Tilmes, S., Filus, M., and Harris, N. R. P., et al.: Airborne
903 measurements of organic bromine compounds in the Pacific tropical tropopause
904 layer, *P. Natl. Acad. Sci. USA*, 112, 13789–13793, doi:10.1073/pnas.1511463112,
905 2015.

906 Newell, R. E., and Gould-Stewart, S.: A stratospheric fountain? *J. Atmos. Sci.*, 38,

907 2789–2796, DOI: 10.1175/1520-0469(1981)038<2789:ASF>2.0.CO;2, 1981.

908 Newton, R., Vaughan, G., Hints, E., Filus, M. T., Pan, L. L., and Honomichl, S., et al.:

909 Observations of ozone-poor air in the tropical tropopause layer, *Atmos. Chem.*

910 *Phys.*, 18, 5157–5171, <https://doi.org/10.5194/acp-18-5157-2018>, 2018.

911 Pan, L. L., Atlas, E. L., Salawitch, R. J., Honomichl, S. B., Bresch, J. F., and Randel,

912 W. J., et al.: The Convective Transport of Active Species in the Tropics

913 (CONTRAST) Experiment, *B. Am. Meteorol. Soc.*, 98(1), 106-128,

914 DOI: 10.1175/BAMS-D-14-00272.1, 2016.

915 Pan, L. L., Honomichl, S. B., Thornberry, T., Rollins, A., Bui, T. P., Pfister, L., and

916 Jensen E. E.: Observational Evidence of Horizontal Transport-Driven

917 Dehydration in the TTL, *Geophys. Res. Lett.*, 46(13), 7848-7856,

918 DOI: 10.1029/2019GL083647, 2019.

919 [Park, M., Randel, W. J., Emmons, L. K. and Livesey, N. J.: Transport pathways of](#)

920 [carbon monoxide in the Asian summer monsoon diagnosed from Model of Ozon](#)

921 [and Related Tracers \(MOZART\), *J. Geophys. Res.*, 144, D08303,](#)

922 [doi:10.1029/2008JD010621, 2009.](#)

923 Qie, K., Qie, X., and Tian, W.: Increasing trend of lightning activity in the South Asia

924 region, *Sci. Bull.*, 66, 78-84, <https://doi.org/10.1016/j.scib.2020.08.033>, 2021.

925 Randel, W. J., and Jensen, E. J.: Physical processes in the tropical tropopause layer

926 and their roles in a changing climate, *Nat. Geosci.*, 6, 169–176,

927 DOI:10.1038/ngeo1733, 2013.

928 Randel, W. J., Park, M., Emmons, L., Kinnison, D., Bernath, P., Walker, K. A., Boone,

929 C., and Pumphrey, H., Asian monsoon transport of pollution to the Stratosphere,

930 *Science*, 328, 611-613, DOI: 10.1126/science.1182274, 2010.

931 Rao, J., Yu, Y., Guo, D., Shi, C., Chen, D., and Hu, D.: Evaluating the Brewer-Dobson

932 circulation and its responses to ENSO, QBO, and the solar cycle in different

933 reanalyses, *Earth Planet. Phys.*, 3(2), 1-16, <http://doi.org/10.26464/epp2019012>,

934 2019.

935 Rayner, N., Parker, D., Horton, E., Folland, C. K., Alexander, L., and Rowell, D. P., et

936 al.: Global analyses of sea surface temperature, sea ice, and night marine air

937 temperature since the late nineteenth century, *J. Geophys. Res.*, 108(D14), 4407,
938 doi:10.1029/2002JD002670, 2003.

939 Rosenlof, K. H. How water enters the stratosphere, *Science*, 302, 1691-1692,
940 doi:10.1126/science.1092703, 2003.

941 Ryu, J., and Lee, S.: Effect of tropical waves on the tropical tropopause transition
942 layer upwelling, *J. Atmos. Sci.*, 67(10), 3130-3148,
943 DOI: 10.1175/2010JAS3434.1, 2010.

944 Saiz-Lopez, A., and von Glasow, R.: Reactive halogen chemistry in the troposphere,
945 *Chem. Soc. Rev.*, 41, 6448–6472, DOI:10.1039/c2cs35208g, 2012.

946 Schoeberl, M. R., Jensen, E. J., Pfister, L., Ueyama, R., Avery, M., and Dessler, A. E.:
947 Convective hydration of the upper troposphere and lower stratosphere, *J.*
948 *Geophys. Res.*, 123(9), 4583-4593, <https://doi.org/10.1029/2018JD028286>, 2018.

949 Sherwood, S. C.: A stratospheric “drain” over the maritime continent, *Geophys. Res.*
950 *Lett.*, 27(5), 677-680, <https://doi.org/10.1029/1999GL010868>, 2000.

951 Shindell, D. T., Pechony, O., Voulgarakis, A., Faluvegi, G., Nazarenko, L., Lamarque,
952 J.-F., Bowman, K., Milly, G., Kovari, B., Ruedy, R., and Schmidt, G. A.:
953 Interactive ozone and methane chemistry in GISS-E2 historical future climate
954 simulations, *Atmos. Chem. Phys.*, 13, 2653-2689,
955 doi:10.5194/acp-13-2653-2013, 2013.

956 Shirley, D., Stanley, W., & Daniel, C.: *Statistics for Research (Third Edition)*, (p. 627),
957 Hoboken, New Jersey: John Wiley & Sons Inc., 2004.

958 Simmons, A. J., Poli, P., Dee, D. P., Berrisford, P., Hersbach, H., Kobayashi, S., and
959 Peubey, C.: Estimating lowfrequency variability and trends in atmospheric
960 temperature using ERA-Interim, *Q. J. Roy. Meteorol. Soc.*, 140, 329 – 353,
961 <https://doi.org/10.1002/qj.2317>, 2014.

962 Sinnhuber, B.-M., Sheode, N., Sinnhuber, M., Chipperfield, M. P., and Feng, W.: The
963 contribution of anthropogenic bromine emissions to past stratospheric ozone
964 trends: a modelling study, *Atmos. Chem. Phys.*, 9, 2863 – 2871,
965 doi:10.5194/acp-9-2863-2009, 2009.

966 Solomon, S., Rosenlof, K. H., Portmann, R. W., Daniel, J. S., Davis, S. M., Sanford, T.

967 J., and Plattner, G.-K.: Contributions of stratospheric water vapor to decadal
968 changes in the rate of global warming, *Science*, 327, 1219-1223,
969 DOI:10.1126/science.1182488, 2010.

970 Tegtmeier, S., Anstey, J., Davis, S., Dragani, R., Harada, Y., Ivanciu, I., Kedzierski, R.
971 P., Krüger, K., Legras, B., Long, C., Wang, J. S., Wargan, K., and Wright, J. S.:
972 Temperature and tropopause characteristics from reanalyses data in the tropical
973 tropopause layer, *Atmos. Chem. Phys.*, 20, 753-770,
974 <https://doi.org/10.5194/acp-20-753-2020>, 2020.

975 Tokinaga, H., Xie, S. P., Deser, C., Kosaka, Y., and Okumura, Y. M.: Slowdown of the
976 Walker circulation driven by tropical Indo-Pacific warming. *Nature*, 491,
977 439–443, DOI: 10.1038/nature11576, 2012.

978 Uma, K. N., Das, S. S., Ratnam, M. V., and Suneeth, K. V.: Assessment of vertical air
979 motion among reanalyses and qualitative comparison with very-high-frequency
980 radar measurements over two tropical stations, *Atmos. Chem. Phys.*, 21,
981 2083-2103, <https://doi.org/10.5194/acp-21-2083-2021>, 2021.

982 Wales, P. A., Salawitch, R. J., Nicely, J. M., Anderson, D. C., Canty, T. P. and Baidar,
983 S., et al.: Stratospheric injection of Brominated very short-lived substances:
984 Aircraft observations in the western Pacific and representation in global models,
985 *J. Geophys. Res.*, 123(10), 5690-5719, <https://doi.org/10.1029/2017JD027978>,
986 2017.

987 Wang, S., Schmidt, J. A., Baidar, S., Coburn, S., Dix, B., and Koenig, T. K., et al.:
988 Active and wide-spread halogen chemistry in the tropical and subtropical free
989 troposphere, *P. Natl. Acad. Sci. USA*, 112, 9281–9286,
990 DOI: 10.1073/pnas.1505142112, 2015.

991 Wang, W., Matthes, K., and Schmidt, T.: Quantifying contributions to the recent
992 temperature variability in the tropical tropopause layer, *Atmos. Chem. Phys.*, 15,
993 5815–5826, doi:10.5194/acp-15-5815-2015, 2015.

994 Wang, W., Matthes, K., Omarani, N.-E., and Latif, M.: Decadal variability of tropical
995 tropopause temperature and its relationship to the Pacific Decadal Oscillation,
996 *Sci. Rep.*, 6, 29537, <https://doi.org/10.1038/srep29537>, 2016.

997 Wang, W., Tian, W., Dhomse, S., Xie, F., Shu, J., and Austin, J.: Stratospheric ozone
998 depletion from future nitrous oxide increases, *Atmos. Chem. Phys.*, 14,
999 12967-12982, doi:10.5194/acp-14-12967-2014, 2014.

1000 Webster, P. J., Lukas, R.: TOGA COARE: the coupled ocean-atmosphere response
1001 experiment, *B. Am. Meteorol. Soc.*, 73(9), 1377-1416,
1002 DOI: 10.1175/1520-0477(1992)073<1377:TCTCOR>2.0.CO;2, 1992.

1003 Webster, P. J., Clayson, C. A., Curry, J. A.: Clouds, radiation, and the diurnal cycle of
1004 sea surface temperature in the tropical western Pacific, *J. Climate*, 8(8),
1005 1712-1730, DOI: 10.1175/1520-0442(1996)009<1712:CRATDC>2.0.CO;2,
1006 1996.

1007 WMO.: Low-cost Sensors for the Measurement of Atmospheric Composition:
1008 Overview of Topic and Future Applications, 2018.

1009 [Xiao, Y., Jacob, D. J., and Turquety, S.: Atmospheric acetylene and its relationship](#)
1010 [with CO as an indicator of air mass age, *J. Geophys. Res.*, 112, D12305,](#)
1011 [doi:10.1029/2006JD008268, 2007.](#)

1012 Xie, F., Li, J., Tian, W., Feng, J., and Huo, Y.: Signals of El Niño Modoki in the
1013 tropical tropopause layer and stratosphere, *Atmos. Chem. Phys.*, 12, 5259-5273,
1014 doi:10.5194/acp-12-5259-2012, 2012.

1015 Xie, F., Li, J., Tian, W., Li, Y., and Feng, J.: Indo-Pacific Warm Pool Area Expansion,
1016 Modoki Activity, and Tropical Cold-Point Tropopause Temperature Variations,
1017 *Sci. Rep.*, 4, 4552, <https://doi.org/10.1038/srep04552>, 2014a.

1018 Xie, F., Li, J., Tian, W., Zhang, J., and Shu, J.: The impacts of two types of El Niño on
1019 global ozone variations in the last three decades, *Adv. Atmos. Sci.*, 31(5),
1020 1113-1126, doi: 10.1007/s00376-013-3166-0, 2014b.

1021 Xie, F., Tian, W., Zhou, X., Zhang, J., Xia, Y., and Lu, J.: Increase in lower
1022 stratospheric water vapor in the past 100 years related to tropical Atlantic
1023 warming, *Geophys. Res. Lett.*, 47, e2020GL090539,
1024 DOI: 10.1029/2020GL090539, 2020.

1025 Zhou, X., Chen, Q., Li, Y., Zhao, Y., Lin, Y., and Jiang, Y.: Impacts of the Indo-Pacific
1026 warm pool on lower stratospheric water vapor: Seasonality and hemispheric

1027 contrasts, J. Geophys. Res., 126, e2020JD034363, DOI: 10.1029/2020JD034363,
1028 2021.

1029

1030 **Figure captions:**

1031 **Fig. 1.** The climatological mean (averaged over 1958-2017) values of 150 hPa w (10^{-2}
1032 m s^{-1}) in [Jan.-Dec. \(a-1\)](#) derived from the JRA55 data.

1033 **Fig. 2.** Trends of vertical velocity and horizontal winds at 150 hPa, 500 hPa, 700 hPa
1034 in NDJFM derived from JRA55, ERA5, and MERRA2 data. The trends of horizontal
1035 winds (arrows, units: $10^{-1} \text{ m s}^{-1} \text{ a}^{-1}$) and vertical velocity (shading, units: $10^{-4} \text{ m s}^{-1} \text{ a}^{-1}$)
1036 at (a) 150 hPa; (d) 500 hPa; and (g) 700 hPa from JRA55 in NDJFM during
1037 1958-2017. (b), (e), and (h) are the same as (a), (d), and (g) but for the results from
1038 ERA5. (c), (f) and (i) are the same as (a), (d), and (g) except that the trends are during
1039 1980-2017 and the wind field data are from MERRA2. The vertical velocity trends
1040 over the dotted regions are statistically significant at the 95% confidence level. The
1041 white areas denote missing values. The black rectangles denote the TWP region
1042 (20°S - 10°N , 100°E - 180°E).

1043 **Fig. 3.** The time series of the standardized intensity of the upward motion over the
1044 tropical western Pacific (20°S - 10°N , 100°E - 180°E) at (a) 150 hPa; (b) 500 hPa; and
1045 (c) 700 hPa extracted from JRA55 (red), ERA5 (black) and MERRA2 (blue) datasets.
1046 The straight lines in each figure indicate the linear trends. The solid lines denote the
1047 linear trends are significant at the 95% confidence level, while the dashed lines denote
1048 the linear trends are significant at the 90% confidence level.

1049 **Fig. 4.** Trends of (a) observed outgoing longwave radiation (OLR, units: $\text{W m}^{-2} \text{ a}^{-1}$)
1050 provided by NOAA during 1974-2017; (b) cold-point tropopause temperature (CPTT,

1051 units: 10^{-1} K a^{-1}) derived from JRA55 data and (c) SST (K a^{-1}) derived from HadISST
1052 during 1958-2017 in NDJFM. (d) The correlation coefficients between the intensity of
1053 the upward motion at 150 hPa over the TWP and SST in NDJFM during 1958-2017
1054 with the linear trends removed. The trends and correlation coefficients over the dotted
1055 regions are statistically significant at the 95% confidence level. The black rectangles
1056 denote the TWP region (20°S - 10°N , 100°E - 180°E).

1057 **Fig. 5.** Same as Fig. 2 but for the Control simulation (a, d, and g), Fixsst simulation (b,
1058 e, and h), and the difference between the simulations (c, f, and i). The vertical velocity
1059 trends over the dotted regions are statistically significant at the 95% confidence level.
1060 The black rectangles denote the TWP region (20°S - 10°N , 100°E - 180°E).

1061 **Fig. 6.** The difference of vertical velocity (shading, units: 10^{-2} m s^{-1}) and horizontal
1062 winds (arrows, units: m s^{-1}) at (a) 150 hPa; (b) 500 hPa; and (c) 700 hPa in NDJFM
1063 between experiments R1 and R2. The differences between vertical velocity over the
1064 dotted regions are statistically significant at the 95% confidence level. The black
1065 rectangles denote the TWP region (20°S - 10°N , 100°E - 180°E).

1066 **Fig. 7.** Same as Fig. 5 but for the trends of (a)-(c) OLR ($\text{W m}^{-2} \text{ a}^{-1}$), (d-f) CPTT
1067 (shading, units: 10^{-1} K a^{-1}) and 100 hPa streamfunction (contour, units: $10^6 \text{ m}^2 \text{ s}^{-1} \text{ a}^{-1}$),
1068 and (g-i) 70 hPa water vapor concentration (units: $10^{-2} \text{ ppmv a}^{-1}$). The trends in (a)-(c)
1069 and (g)-(i) over the dotted regions are statistically significant at the 95% confidence
1070 level. The CPTT trends in (d)-(f) over the dotted regions are statistically significant at
1071 the 95% confidence level. The black rectangles denote the TWP region (20°S - 10°N ,
1072 100°E - 180°E).

1073 **Fig. 8.** The trends of CO derived from the MOPITT and MLS data. (a) The trends of
1074 CO (10^{-1} ppbv a^{-1}) at 215 hPa using MLS data in NDJFM during 2005-2017. (b) The
1075 trends of CO (10^{-1} ppbv a^{-1}) at 200 hPa using MOPITT data in NDJFM during
1076 2000-2017. The trends of CO over the dotted region are statistically significant at the
1077 90% confidence level.

1078 **Fig. 9.** The trends of 150 hPa CO concentration (10^{-4} ppmv a^{-1}) from (a) Control
1079 simulation; (b) Fixsst simulation; and (c) difference between the Control simulation
1080 and the Fixsst simulation in NDJFM during 1958-2017. The trends in (a)-(c) over the
1081 dotted regions are statistically significant at the 95% confidence level. The black
1082 rectangles denote the TWP region (20°S - 10°N , 100°E - 180°E).

1083 **Fig. 10.** Latitude-pressure cross sections of the trends of (a)-(c) zonal mean CO
1084 concentration (10^{-4} ppmv a^{-1}) and (d)-(f) CO concentration (10^{-4} ppmv a^{-1}) over the
1085 TWP (100°E - 180°E) in NDJFM during 1958-2017 in the Control simulation and
1086 Fixsst simulation as well as their difference. (a) and (d) are the CO trends in the
1087 Control simulation. (b) and (e) are the results in the Fixsst simulation. (c) and (f) are
1088 the results derived from the difference between the Control and Fixsst simulations.
1089 The trends over the dotted regions are statistically significant at the 95% confidence
1090 level.

1091 **Fig. 11.** Same as Fig. 10 but for the trends of tropospheric w (10^{-4} m s^{-1} a^{-1}) and v (10^{-1}
1092 m s^{-1} a^{-1}). The shadings denote the trends of the w (10^{-4} m s^{-1} a^{-1}). The trends over the
1093 dotted regions are statistically significant at the 90% confidence level.

1094 **Fig. 12.** Trends of the BDC (vectors, units in the horizontal and vertical components

1095 are 10^{-2} and $10^{-5} \text{ m s}^{-1} \text{ a}^{-1}$, respectively) calculated using the TEM formula from (a)
1096 JRA55; (b) Control simulation; (c) Fixsst simulation; and (d) difference between the
1097 Control simulation and the Fixsst simulation in NDJFM during 1958-2017. The
1098 shadings are the trends of the w^* ($10^{-5} \text{ m s}^{-1} \text{ a}^{-1}$). The trends of the vertical velocity
1099 over the dotted regions are statistically significant at the 90% confidence level.

1100

Tables:

1101

1102

Table 1. Basic specifications of JRA55, ERA5, and MERRA2 used in this study.

<u>Name</u>	<u>Organization</u>	<u>Time period</u>	<u>Spatial resolution</u>	<u>Temporal resolution</u>	<u>Data assimilation</u>
<u>JRA55</u>	<u>JMA</u>	<u>1958-present</u>	<u>55 km; L60</u>	<u>6-hourly</u>	<u>4D-Var</u>
<u>ERA5</u>	<u>ECMWF</u>	<u>1950-present</u>	<u>31 km; L137</u>	<u>hourly</u>	<u>4D-Var</u>
<u>MERRA2</u>	<u>NASA</u>	<u>1980-present</u>	<u>0.5°×0.625°;</u>	<u>3-hourly</u>	<u>3D-Var</u>
	<u>GMAO</u>		<u>L72</u>		

1103

1104

1105 **Table 2. Description of simulations with WACCM4.**

<u>Experiment</u>	<u>Description</u>
<u>Control</u>	<u>Transient simulation. Observed greenhouse gases and solar irradiances. Prescribed SST forcing using observed SST.</u>
<u>Fixsst</u>	<u>Transient simulation. Observed greenhouse gases and solar irradiances. Prescribed SST forcing using monthly mean climatology from 1958 to 2017.</u>
<u>R1</u>	<u>Time-slice simulation. SSTs prescribed as the climatological mean of 1998-2017 over the region 20°S-20°N, 120°E-160°E in NDJFM, but fixed as climatological mean of 1958-2017 over other regions.</u>
<u>R2</u>	<u>Same as R1, but the SSTs over the region 20°S-20°N, 120°E-160°E are prescribed as the climatological mean SSTs during 1958-1977.</u>

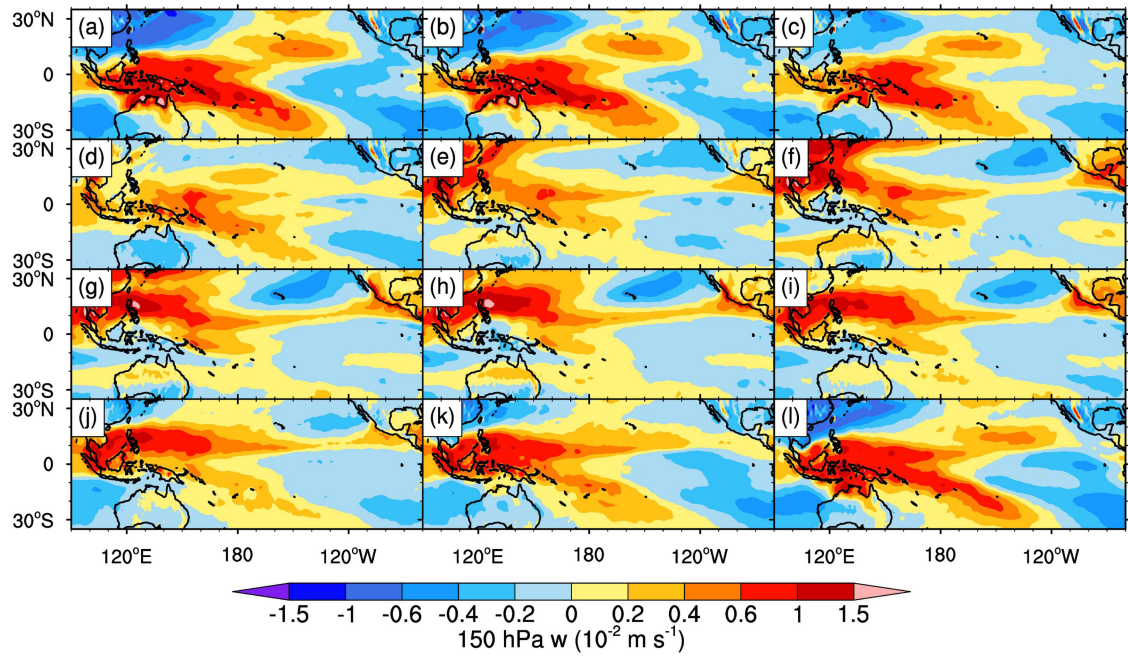
1106

1107 **Table 3.** The trends of the upward motion over the TWP at 150 hPa, 500 hPa, and 700
 1108 hPa in NDJFM during 1958-2017 from JRA55, ERA5, MERRA2, Control simulation
 1109 and Fixsst simulation. And the trends of 150 hPa CO from the Control and Fixsst
 1110 simulations.

	<u>JRA55</u>	<u>ERA5</u>	<u>MERRA2</u>	<u>Control</u>	<u>Fixsst</u>
<u>150 hPa</u>	<u>$3.0 \pm 1.2 \times 10^9$</u>	<u>$1.3 \pm 1.2 \times 10^9$</u>	<u>$3.0 \pm 2.8 \times 10^9$</u>	<u>$2.0 \pm 1.2 \times 10^9$</u>	<u>$-4.8 \pm 6.4 \times 10^8$</u>
<u>Upward</u>	<u>kg s^{-1}</u>	<u>kg s^{-1}</u>	<u>kg s^{-1}</u>	<u>kg s^{-1}</u>	<u>kg s^{-1}</u>
<u>motion</u>	<u>decade^{-1}</u>	<u>decade^{-1}</u>	<u>decade^{-1}</u>	<u>decade^{-1}</u>	<u>decade^{-1}</u>
<u>500 hPa</u>	<u>$4.6 \pm 2.6 \times 10^9$</u>	<u>$2.5 \pm 2.5 \times 10^9$</u>	<u>$5.4 \pm 5.3 \times 10^9$</u>	<u>$3.5 \pm 2.4 \times 10^9$</u>	<u>$-1.0 \pm 1.3 \times 10^9$</u>
<u>Upward</u>	<u>kg s^{-1}</u>	<u>kg s^{-1}</u>	<u>kg s^{-1}</u>	<u>kg s^{-1}</u>	<u>kg s^{-1}</u>
<u>motion</u>	<u>decade^{-1}</u>	<u>decade^{-1}</u>	<u>decade^{-1}</u>	<u>decade^{-1}</u>	<u>decade^{-1}</u>
<u>700 hPa</u>	<u>$2.9 \pm 1.7 \times 10^9$</u>	<u>$1.9 \pm 1.6 \times 10^9$</u>	<u>$3.9 \pm 3.8 \times 10^9$</u>	<u>$1.8 \pm 1.4 \times 10^9$</u>	<u>$-6.3 \pm 8.1 \times 10^8$</u>
<u>Upward</u>	<u>kg s^{-1}</u>	<u>kg s^{-1}</u>	<u>kg s^{-1}</u>	<u>kg s^{-1}</u>	<u>kg s^{-1}</u>
<u>motion</u>	<u>decade^{-1}</u>	<u>decade^{-1}</u>	<u>decade^{-1}</u>	<u>decade^{-1}</u>	<u>decade^{-1}</u>
<u>150 hPa</u>	<u>==</u>	<u>==</u>	<u>==</u>	<u>3.4 ppbv</u>	<u>3.2 ppbv</u>
<u>CO</u>				<u>decade^{-1}</u>	<u>decade^{-1}</u>

1111

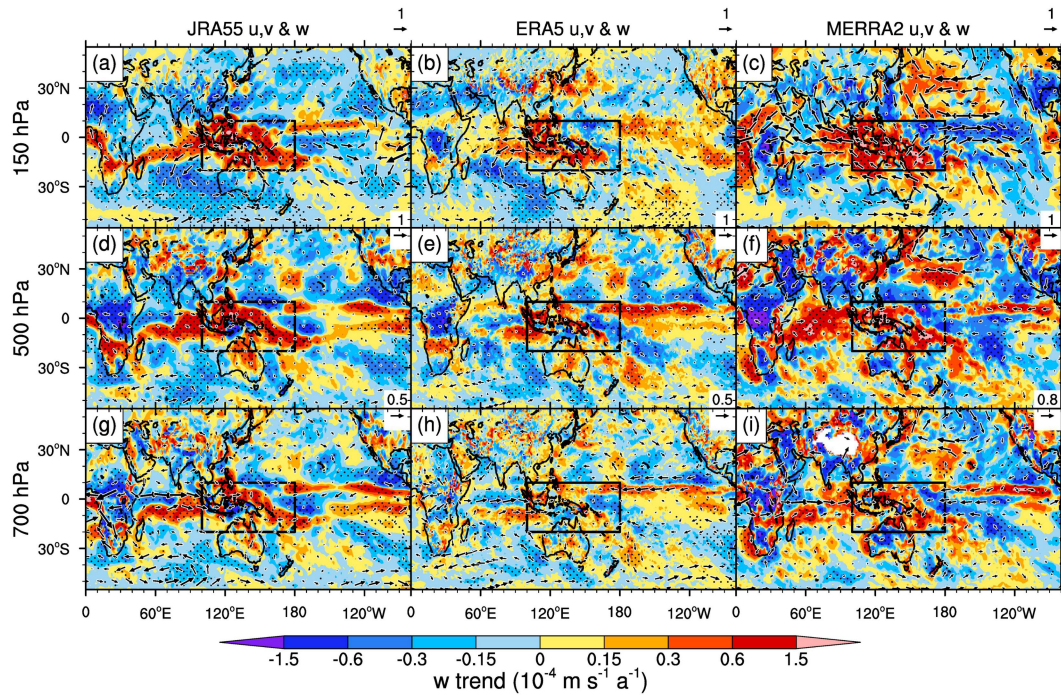
1112 **Figures**



1113

1114 **Fig. 1.** The climatological mean (averaged over 1958-2017) values of 150 hPa w (10^{-2}
1115 m s^{-1}) in Jan.-Dec. (a-l) derived from the JRA55 reanalysis data.

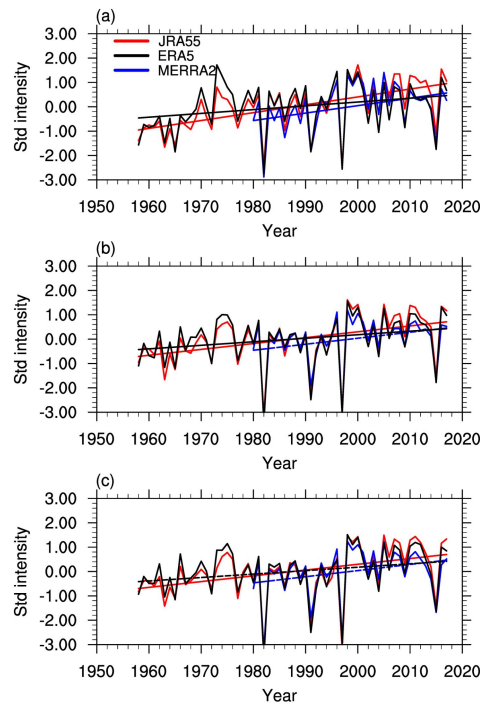
1116



1117

1118 **Fig. 2.** Trends of vertical velocity and horizontal winds at 150 hPa, 500 hPa, 700 hPa
 1119 in NDJFM derived from JRA55, ERA5, and MERRA2 data. The trends of horizontal
 1120 winds (arrows, units: $10^{-1} \text{ m s}^{-1} \text{ a}^{-1}$) and vertical velocity (shading, units: $10^{-4} \text{ m s}^{-1} \text{ a}^{-1}$)
 1121 at (a) 150 hPa; (d) 500 hPa; and (g) 700 hPa from JRA55 in NDJFM during
 1122 1958-2017. (b), (e), and (h) are the same as (a), (d), and (g) but for the results from
 1123 ERA5. (c), (f) and (i) are the same as (a), (d), and (g) except that the trends are during
 1124 1980-2017 and the wind field data are from MERRA2. The vertical velocity trends
 1125 over the dotted regions are statistically significant at the 95% confidence level. The
 1126 white areas denote missing values. The black rectangles denote the TWP region
 1127 (20°S - 10°N , 100°E - 180°E).

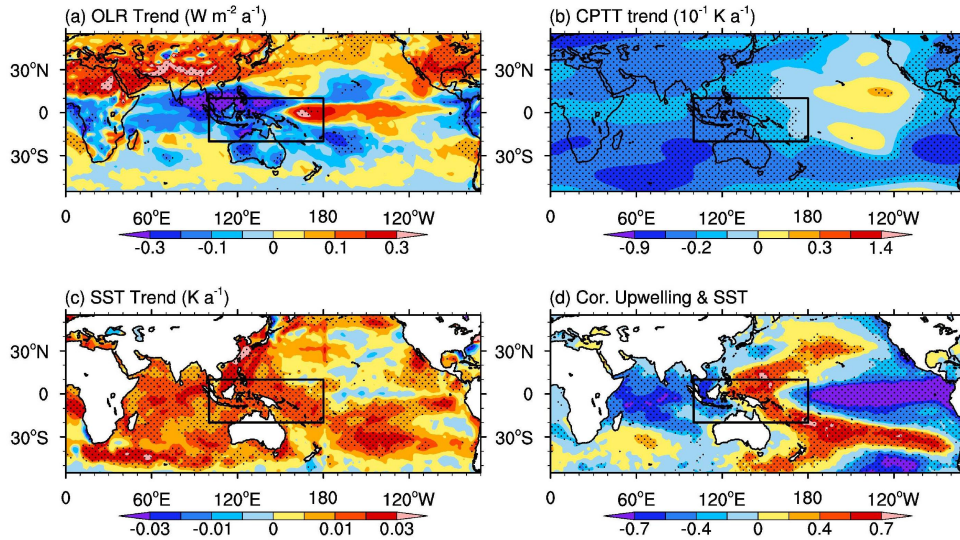
1128



1130

1131 **Fig. 3.** The time series of the standardized intensity of the upward motion over the
 1132 tropical western Pacific (20°S - 10°N , 100°E - 180°E) at (a) 150 hPa; (b) 500 hPa; and
 1133 (c) 700 hPa extracted from JRA55 (red), ERA5 (black) and MERRA2 (blue) datasets.
 1134 The straight lines in each figure indicate the linear trends. The solid lines denote the
 1135 linear trends are significant at the 95% confidence level, while the dashed lines denote
 1136 the linear trends are significant at the 90% confidence level.

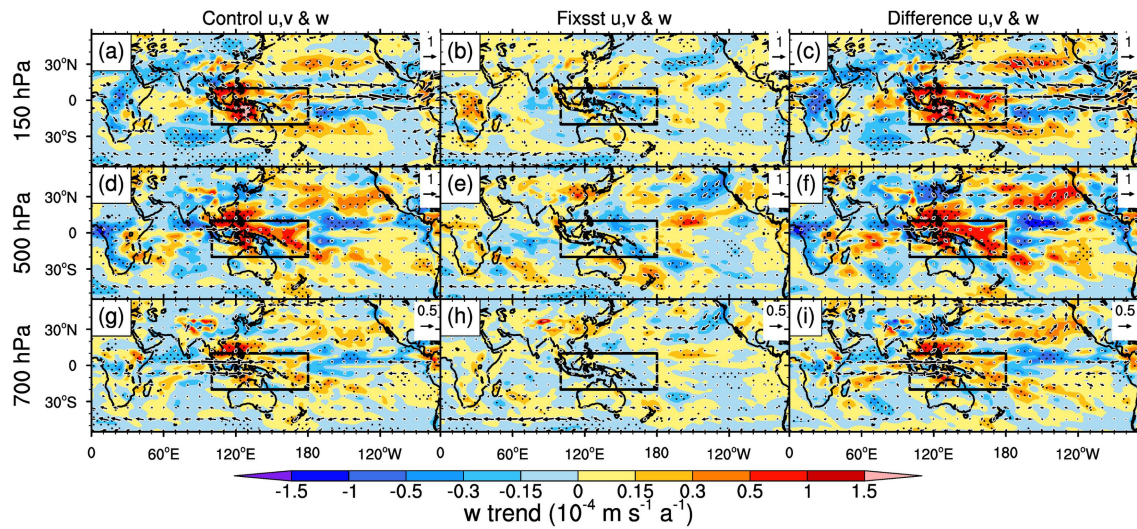
1137



1138

1139 **Fig. 4.** Trends of (a) observed outgoing longwave radiation (OLR, units: $W m^{-2} a^{-1}$)
 1140 provided by NOAA during 1974-2017; (b) cold-point tropopause temperature (CPTT,
 1141 units: $10^{-1} K a^{-1}$) derived from JRA55 data and (c) SST ($K a^{-1}$) derived from HadISST
 1142 during 1958-2017 in NDJFM. (d) The correlation coefficients between the intensity of
 1143 the upward motion at 150 hPa over the TWP and SST in NDJFM during 1958-2017
 1144 with the linear trends removed. The trends and correlation coefficients over the dotted
 1145 regions are statistically significant at the 95% confidence level. The black rectangles
 1146 denote the TWP region (20°S-10°N, 100°E-180°E).

1147



1148

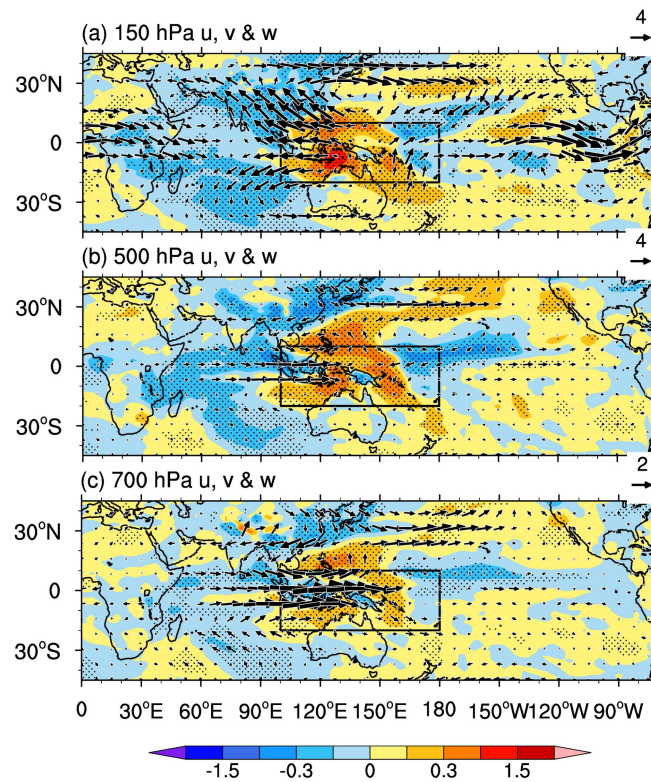
1149 **Fig. 5.** Same as Fig. 2 but for the Control simulation (a, d, and g), Fixsst simulation (b,

1150 e, and h), and the difference between the simulations (c, f, and i). The vertical velocity

1151 trends over the dotted regions are statistically significant at the 95% confidence level.

1152 The black rectangles denote the TWP region (20°S-10°N, 100°E-180°E).

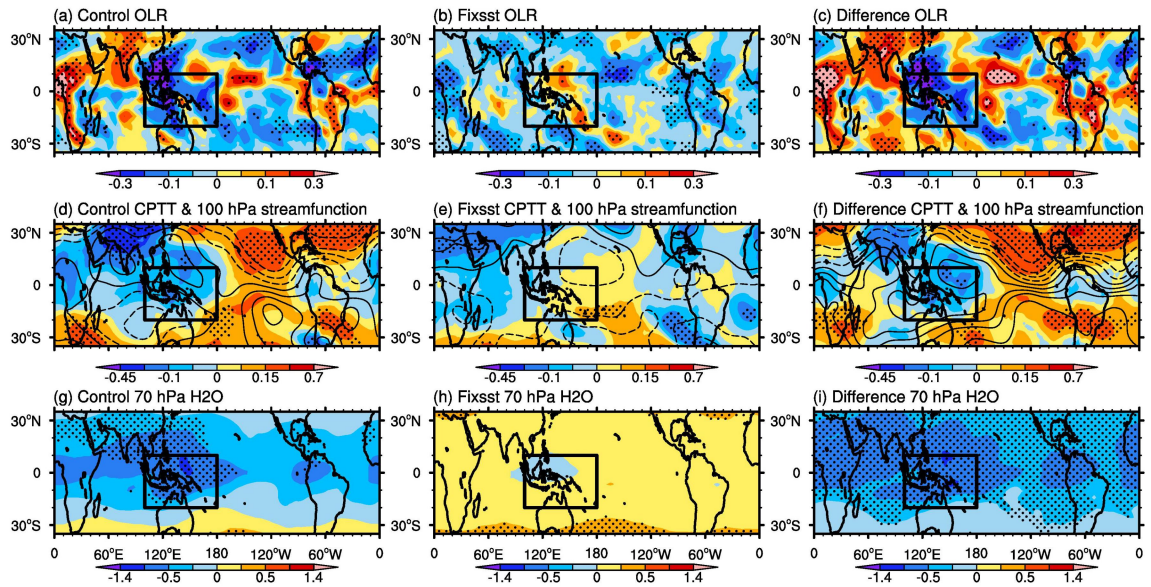
1153



1155

1156 **Fig. 6.** The difference of vertical velocity (shading, units: 10^{-2} m s^{-1}) and horizontal
 1157 winds (arrows, units: m s^{-1}) at (a) 150 hPa; (b) 500 hPa; and (c) 700 hPa in NDJFM
 1158 between experiments R1 and R2. The differences between vertical velocity over the
 1159 dotted regions are statistically significant at the 95% confidence level. The black
 1160 rectangles denote the TWP region (20°S - 10°N , 100°E - 180°E).

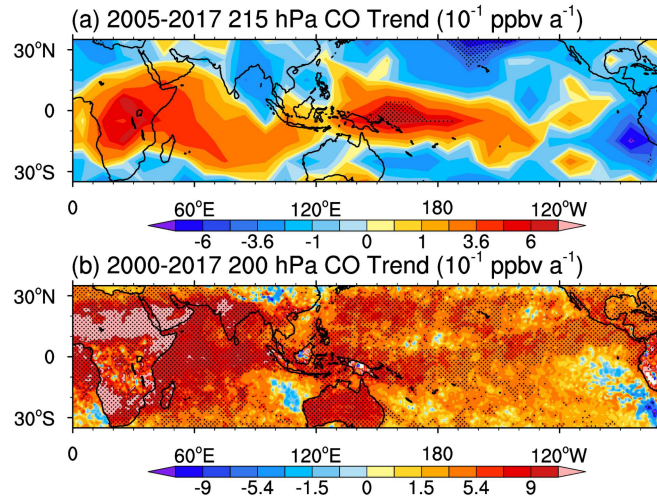
1161



1162

1163 **Fig. 7.** Same as Fig. 5 but for the trends of (a)-(c) OLR ($\text{W m}^{-2} \text{a}^{-1}$), (d-f) CPTT
 1164 (shading, units: 10^{-1}K a^{-1}) and 100 hPa streamfunction (contour, units: $10^6 \text{m}^2 \text{s}^{-1} \text{a}^{-1}$),
 1165 and (g-i) 70 hPa water vapor concentration (units: $10^{-2} \text{ppmv a}^{-1}$). The trends in (a)-(c)
 1166 and (g)-(i) over the dotted regions are statistically significant at the 95% confidence
 1167 level. The CPTT trends in (d)-(f) over the dotted regions are statistically significant at
 1168 the 95% confidence level. The black rectangles denote the TWP region (20°S - 10°N ,
 1169 100°E - 180°E).

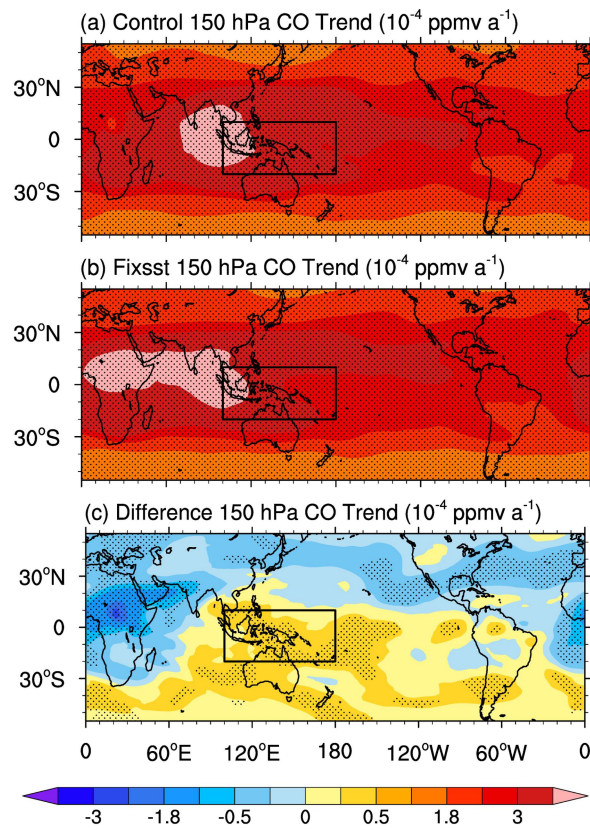
1170



1171

1172 **Fig. 8.** The trends of CO derived from the MOPITT and MLS data. (a) The trends of
 1173 CO (10^{-1} ppbv a^{-1}) at 215 hPa using MLS data in NDJFM during 2005-2017. (b) The
 1174 trends of CO (10^{-1} ppbv a^{-1}) at 200 hPa using MOPITT data in NDJFM during
 1175 2000-2017. The trends of CO over the dotted region are statistically significant at the
 1176 90% confidence level.

1177

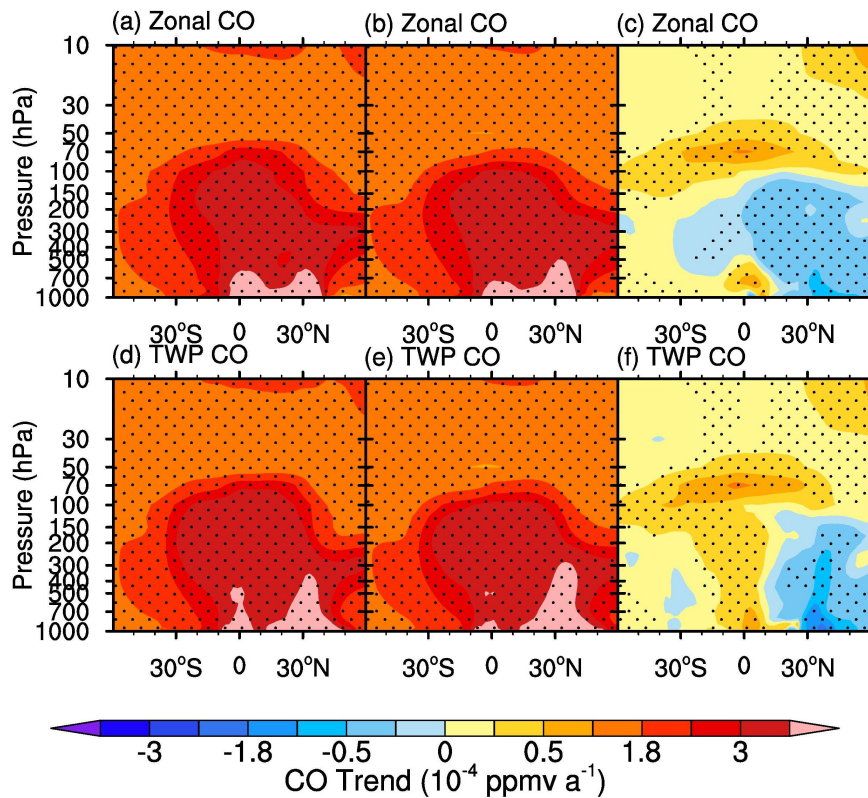


1179

1180 **Fig. 9.** The trends of 150 hPa CO concentration (10^{-4} ppmv a^{-1}) from (a) Control
 1181 simulation; (b) Fixsst simulation; and (c) difference between the Control simulation
 1182 and the Fixsst simulation in NDJFM during 1958-2017. The trends in (a)-(c) over the
 1183 dotted regions are statistically significant at the 95% confidence level. The black
 1184 rectangles denote the TWP region (20°S - 10°N , 100°E - 180°E).

1185

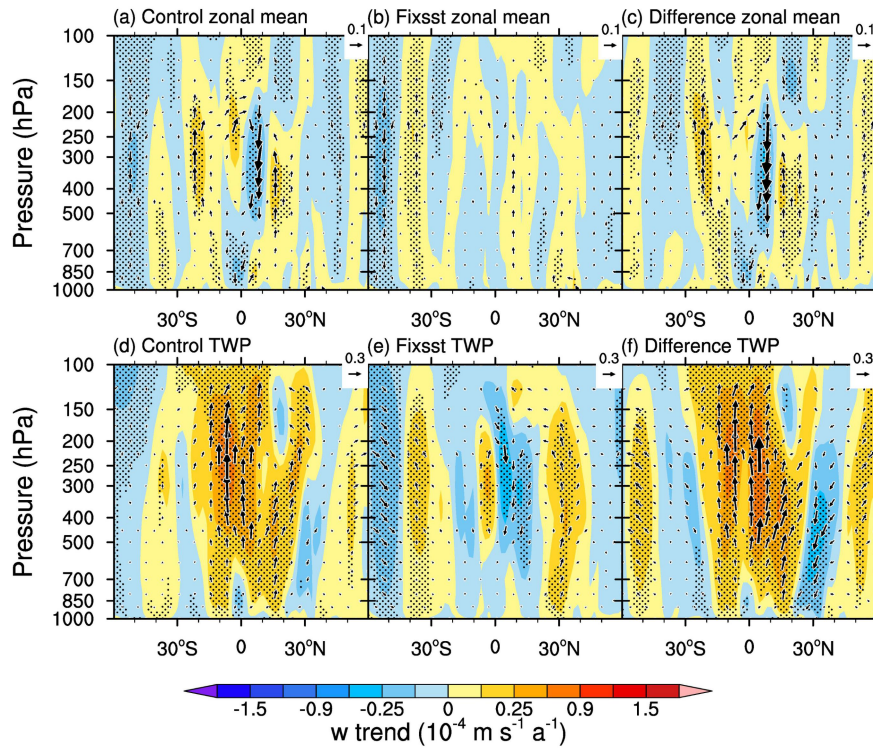
1186



1188

1189 **Fig. 10.** Latitude-pressure cross sections of the trends of (a)-(c) zonal mean CO
 1190 concentration (10^{-4} ppmv a^{-1}) and (d)-(f) CO concentration (10^{-4} ppmv a^{-1}) over the
 1191 TWP (100°E - 180°E) in NDJFM during 1958-2017 in the Control simulation and
 1192 Fixsst simulation as well as their difference. (a) and (d) are the CO trends in the
 1193 Control simulation. (b) and (e) are the results in the Fixsst simulation. (c) and (f) are
 1194 the results derived from the difference between the Control and Fixsst simulations.
 1195 The trends over the dotted regions are statistically significant at the 95% confidence
 1196 level.

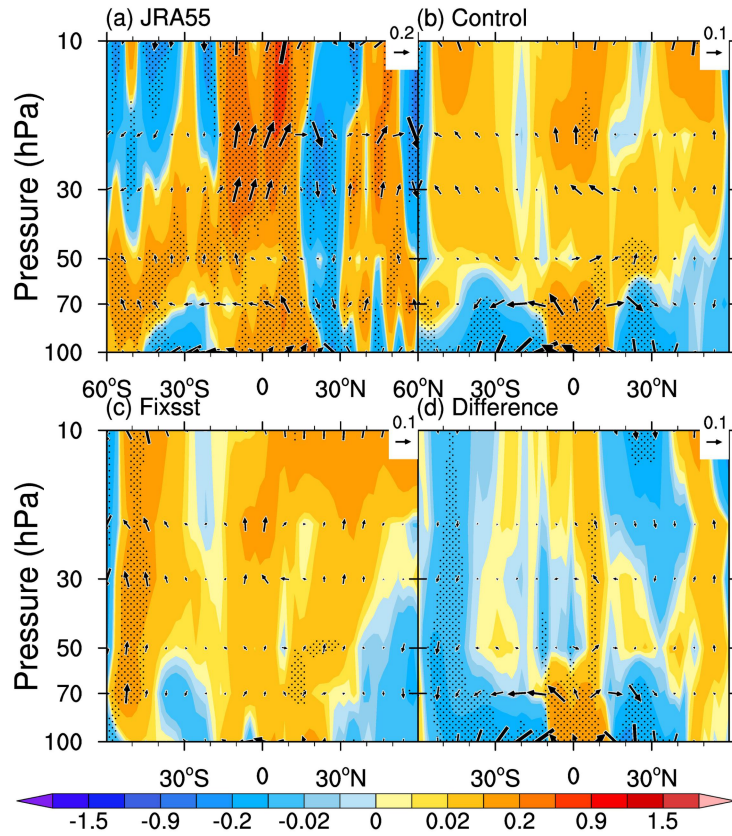
1197



1198

1199 **Fig. 11.** Same as Fig. 10 but for the trends of tropospheric w ($10^{-4} \text{ m s}^{-1} \text{ a}^{-1}$) and v (10^{-1}
 1200 $\text{ m s}^{-1} \text{ a}^{-1}$). The shadings denote the trends of the w ($10^{-4} \text{ m s}^{-1} \text{ a}^{-1}$). The trends over the
 1201 dotted regions are statistically significant at the 90% confidence level.

1202



1203

1204 **Fig. 12.** Trends of the BDC (vectors, units in the horizontal and vertical components
 1205 are 10^{-2} and 10^{-5} $\text{m s}^{-1} \text{a}^{-1}$, respectively) calculated using the TEM formula from (a)
 1206 JRA55; (b) Control simulation; (c) Fixsst simulation; and (d) difference between the
 1207 Control simulation and the Fixsst simulation in NDJFM during 1958-2017. The
 1208 shadings are the trends of the w^* (10^{-5} $\text{m s}^{-1} \text{a}^{-1}$). The trends of the vertical velocity
 1209 over the dotted regions are statistically significant at the 90% confidence level.

1210